

Chapter 10

Numerical Study on the 4.2–2–1 Ellipsoid

The format of this chapter is similar to that of Chapter 9 without the need for details of the UDFs, other code, nor turbulence models. The initial part of this chapter discusses the geometry and the mesh used for the computational study of the ellipsoid. Sections 10.1 and 10.2 each examine the computational results for a single Reynolds number at incidences of -0.2° and -10.2° respectively. Turbulence and total pressure measurements in the wake of the ellipsoid at an incidence of -10.2° are compared with calculations in Section 10.3. Section 10.4 compares the measured and calculated results for the ellipsoid at an incidence of -10.2° with the boundary layer tripped. The force and moment calculations from the previous sections are compared to the measured data in Section 10.5; the CFD is used to examine the sensitivity of these results.

The Fluent preprocessor, Gambit was used to create the mesh for the ellipsoid, sting, foil support and upper limb. The technique of using an offset volume was again used to allow fine control of the mesh in these regions. The main difference between the mesh for the ellipsoid and the spheroid is that the gap between the ellipsoid and the sting along with the associated internal volume was included in all cases. This additional detail was always included as the flatter shape results in the hole for the sting reaching further upstream. Figs. 10.1 and 10.2 show the offset volume used around the ellipsoid and the modified sting. Fig. 10.2 shows the surface mesh and internal volume. For the measurements on the ellipsoid the larger diameter portion of the sting was extended upstream for increased stiffness to allow for the extra mass of the internal balance. As a new sting was required to accommodate the internal balance the lower part of the foil, which is an integral part of the sting, was also modified so that the flow

downstream of the foil was more two-dimensional. These modifications have been included in the CFD model. It is also worth noting that care was required with the construction of the ellipsoidal shape. Gambit does not have a native ellipsoid surface or volume, so external CAD packages were examined to provide the surface. Two of these packages were found to create a surface with apparent distortions. The only significant difference between the topology of this mesh and that used on the spheroid is the triangular prism at the rear of the ellipsoid that wraps around the sting. A triprimitive mesh is used on the triangular surface of this volume and projected around the sting to form the volume mesh. A reduced density of cells in the streamwise direction at the outer surface of the offset volume results from this topology. This reduces the aspect ratio of the faces on the outer surface and allows for less skew in the pyramid cells on the surface and their adjacent tetrahedral cells that are used outside the offset volume.

Given the limited success the technique of using predefined regions of laminar and turbulent boundary layers demonstrated in the previous chapter, the range of numerical solutions compared with the measured results for the ellipsoid is reduced. The focus is on the open separations (as these were observed on the ellipsoid but not the spheroid), the wake and the force results.

Grid sensitivity with a fully turbulent boundary layer was examined using three meshes with the ellipsoid at $\alpha = -10.2^\circ$. The resolution of the mesh in the volume surrounding the ellipsoid is listed in Table 10.1.

grid name	normal intervals	azimuthal intervals ^a	longitudinal intervals			C_D^b	C_L^b	C_M^b
			front half	rear half	gap			
<i>Elli_Grid-10A</i>	94	48	64	66	12	0.0430	0.1456	0.1265
<i>Elli_Grid-10B</i>	94	64	90	92	16	0.0423	0.1439	0.1270
<i>Elli_Grid-10C</i>	94	96	136	138	24	0.0421	0.1438	0.1270
<i>Elli_Grid-10B^c</i>	94	64	90	92	16	0.0430	0.1442	0.1269

^a These intervals distributed over 180° .

^b Force and moments calculated over 360° .

^c The internal region was replaced with a solid so the smooth ellipsoidal surface joins the sting. The area over which the load is calculated is restricted to the same area as the cases with the gap.

Table 10.1: Grid resolution on and normal to ellipsoid surface and loads calculated using realisable $k-\varepsilon$ turbulence model for 4.2–2–1 ellipsoid at -10.2° incidence with $Re_l = 4.0 \times 10^6$.

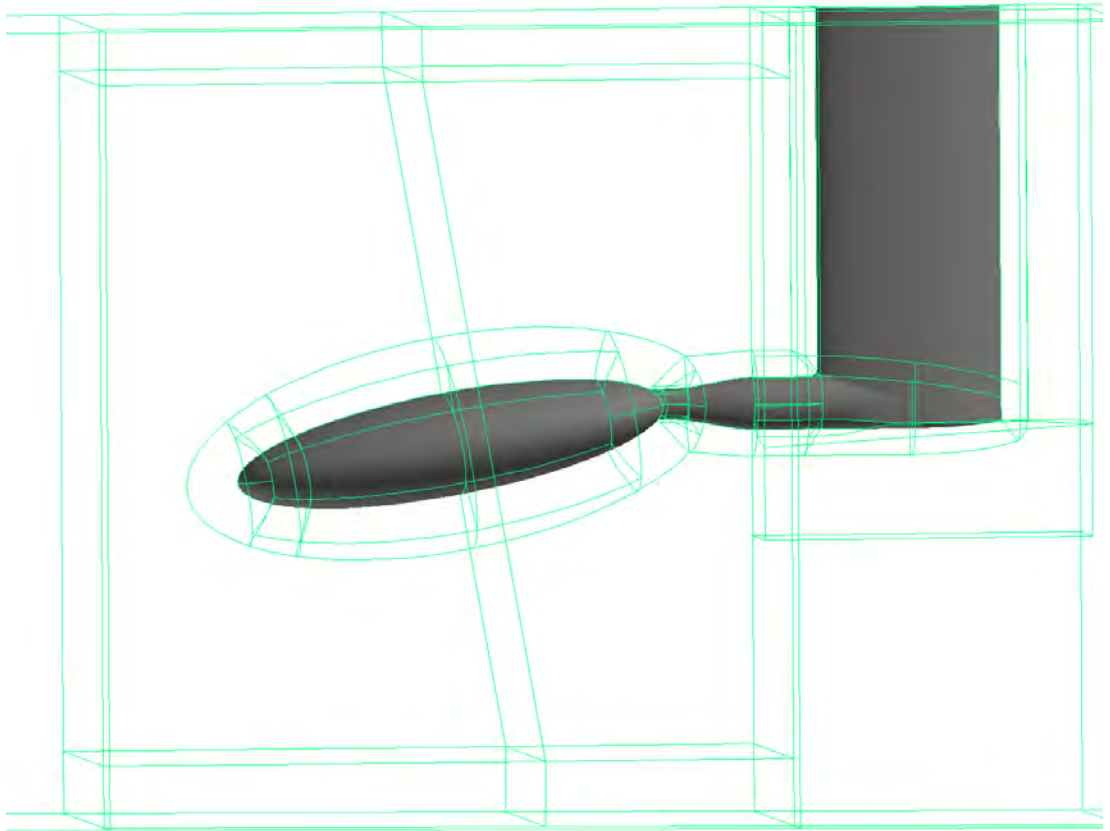


Figure 10.1: Volume geometry for ellipsoid at $\alpha = -10.2^\circ$. The triangular prism wrapped around the sting at the rear of the ellipsoid is used to minimise the number of cells in the streamwise direction at the outer surface of the offset volume.

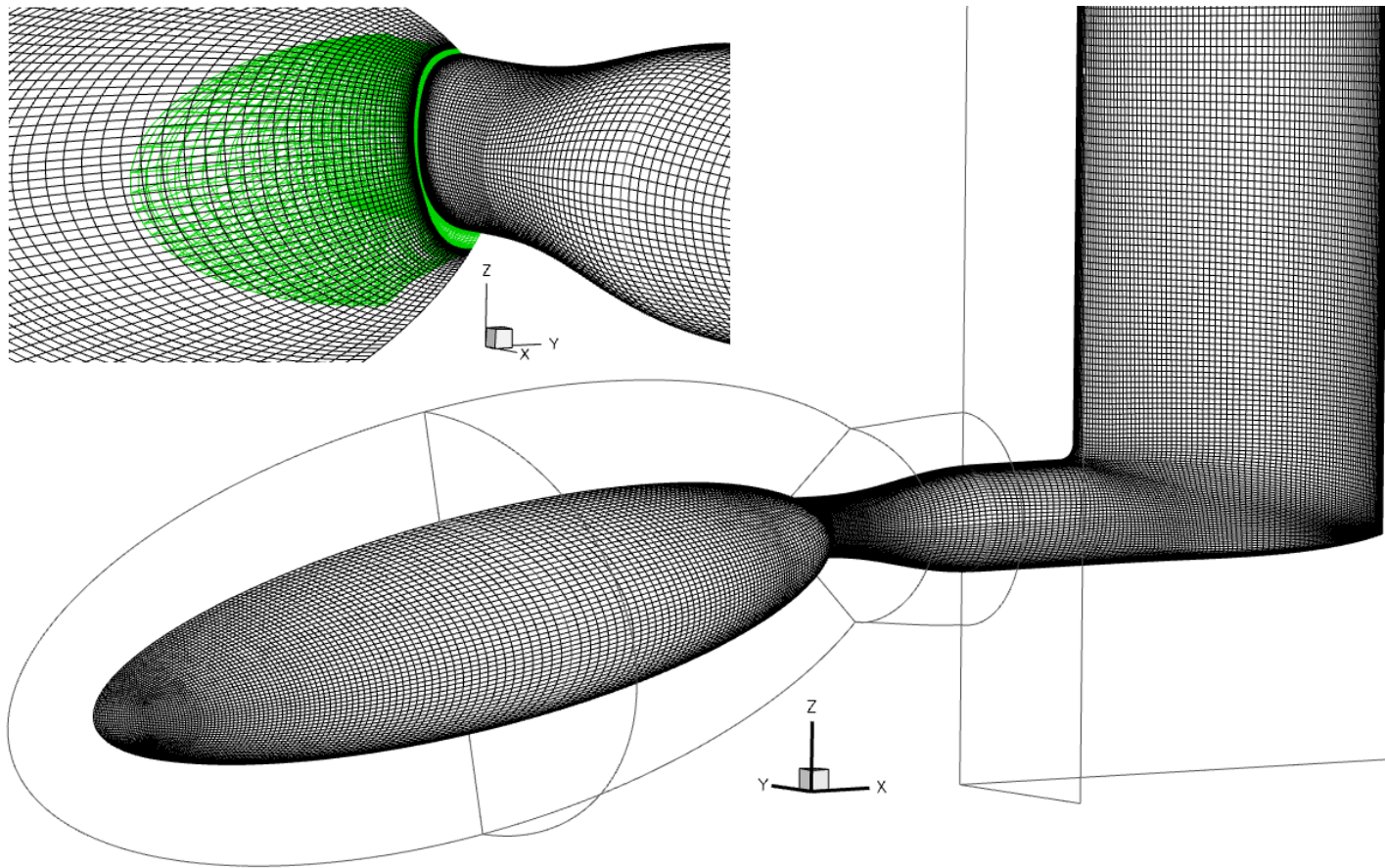


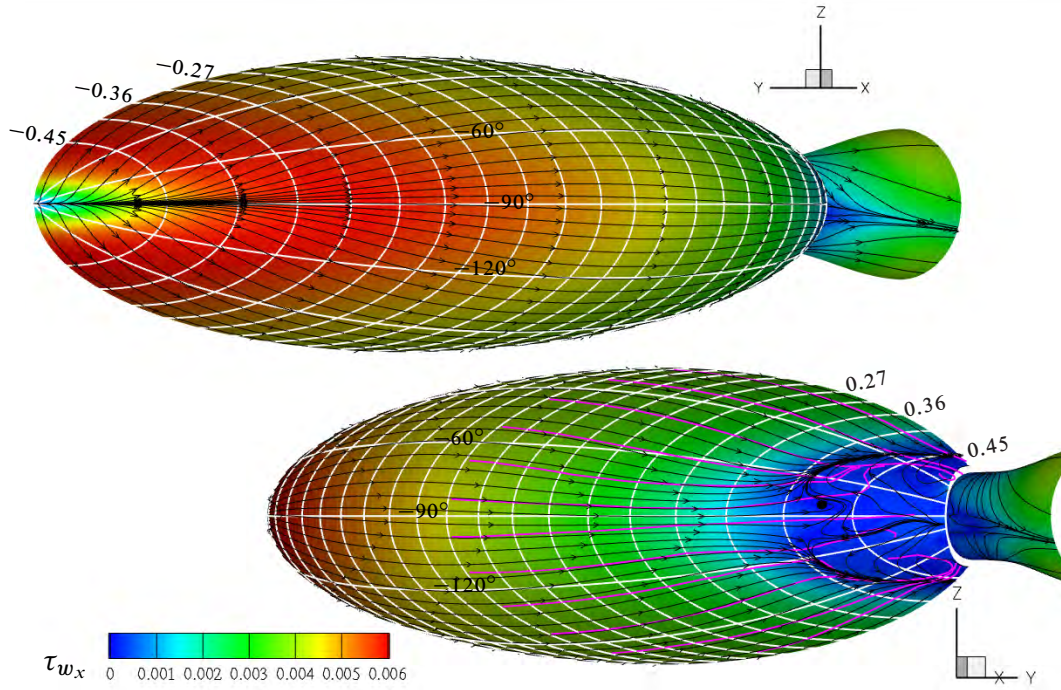
Figure 10.2: Surface mesh for ellipsoid at $\alpha = -10.2^\circ$, *Elli_Grid-10B*. An internal volume shown in green was used for all meshes.

10.1 Results and Discussions for $\alpha = -0.2^\circ$

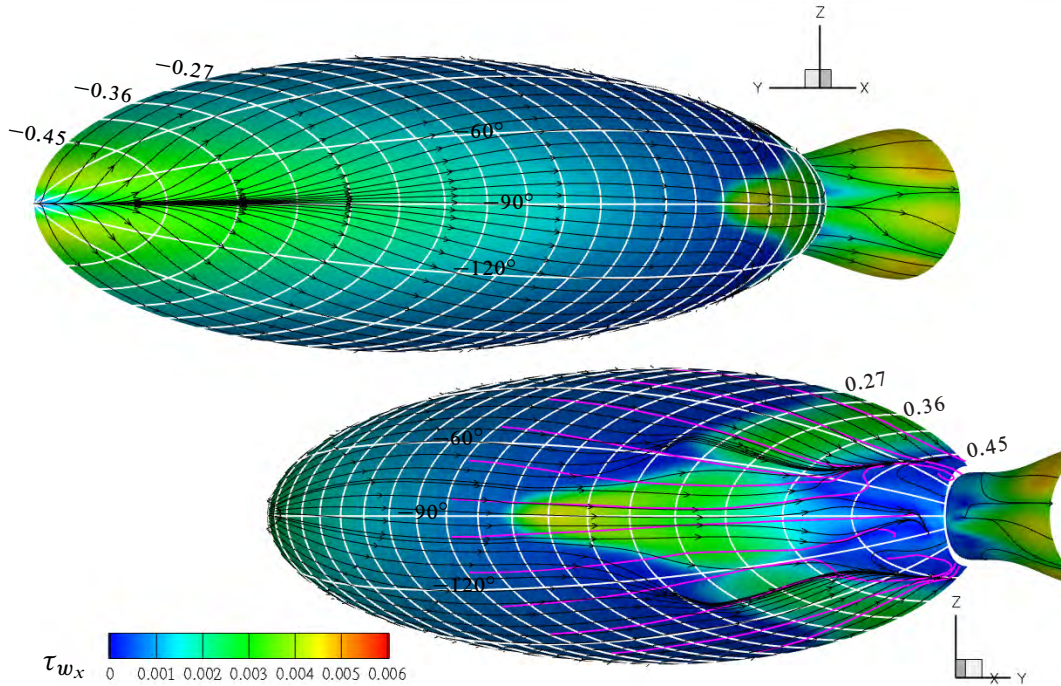
The numerical investigation at this incidence was limited to use of the realisable $k-\varepsilon$ turbulence model. The grid resolution of *Elli_Grid_0B* was the same as that for *Elli_Grid_10B*. For the ellipsoid at $Re_l = 2.5 \times 10^6$ with the region of implemented laminar boundary layer determined from the measured boundary layer, laminar separation without reattachment occurred prior to the start of the turbulent region except on the flank. This problem did not occur for the simulations at $Re_l = 3.0 \times 10^6$ so for this incidence comparisons are made between the computed results at $Re_l = 2.5 \times 10^6$ and $Re_l = 3.0 \times 10^6$ and the measured results at $Re_l = 2.5 \times 10^6$. Given that the flow visualisation results for $Re_l = 2.5 \times 10^6$ and $Re_l = 4.0 \times 10^6$ (Figs. 7.27 and 7.28 respectively) show similar patterns in the surface streamlines it was felt that this comparison could be made at least for the flow visualisation.

Calculated results show the size of the separated region to be greater than measured when the laminar region is not implemented, as shown in Fig. 10.3(a). The extents of attached flow on the horizontal and vertical symmetry planes, observed in the flow visualisation, were not calculated. Near the vertical symmetry plane ($y_{bc} = 0$) the flow is observed to stay attached until the end of the model, while on the horizontal symmetry plane the flow stays attached until $x_{bc} \approx 0.48$. The calculated and measured regions of separated flow between $-30^\circ \leq \varphi_e \leq -150^\circ$ are a close match with the laminar region implemented; however, the attachment of the flow near the vertical symmetry plane was not calculated. The extended length of flow near the $z_{bc} = 0$ plane seen in both the visualisation and this calculation with the laminar region implemented may be explained with similar reasoning to the extended length of attachment observed on the suction side of the spheroid near the vertical symmetry plane for $\alpha = -10.2^\circ$. In this case however the surface curvature rather than the incidence of the model creates the pressure gradient normal to the flow direction at the boundary layer edge. This pressure gradient results in a crossflow that reduces the accumulation of low inertia fluid on the $z_{bc} = 0$ plane. The significant increase in surface shear stress in the fully turbulent case is evident.

The comparison of calculated and measured surface C_p in Fig. 10.4 show a close match between results over the upstream 60% of the ellipsoid; all the measured points in this region were in a laminar boundary layer. The calculations for $Re_l = 2.5 \times 10^6$ with the laminar regions implemented show the oscillations associated with the premature separation of the laminar boundary layer. The calculations for the fully turbulent case at $Re_l = 3.0 \times 10^6$ show the closest match to the measured C_p . With the laminar region implemented, the calculated pressure recovery at the base is greater than measured. This occurs even near the vertical symmetry plane where it is unexpected, given that the extent of the calculated attached flow in this region was less than that seen in the flow visualisation. The measured base C_p does show



(a) Fully turbulent. The size of the calculated separation region at the rear is larger than that seen in the flow visualisation (Fig. 7.27). The extended length of attached boundary layer near $\varphi_e = -90^\circ$ observed in the flow visualisation and apparent in the pressure distributions is not calculated.



(b) Laminar region implemented. The size of the separation region is closer to that observed. These calculations show the attachment of the boundary layer near $\varphi_e = -90^\circ$ extends to a similar extent as observed in the flow visualisation.

Figure 10.3: Computed surface streamlines on 4.2-2-1 ellipsoid using realisable $k-\varepsilon$ turbulence model with and without laminar regions, $Re_l = 3.0 \times 10^6$, $\alpha = -0.2^\circ$, *Elli_Grid_0B*. Contours of wall shear stress show a significant difference when the measured laminar region is implemented. Surface streamlines from flow visualisation for $Re_l = 2.5 \times 10^6$ shown in magenta; calculated surface streamlines in black ($Re_l = 3.0 \times 10^6$).

a significant decrease, from 0.30 to 0.19, as Re_l increases from 2.0×10^6 to $Re_l = 4.0 \times 10^6$; so C_p is showing a significant variation even though the observed surface streamlines are similar.

Given that the gap between the sting and ellipsoid was modelled, this opportunity was taken to examine the assumption that the internal pressure measurement would provide a reasonable estimate of the pressure at the end of the model. Fig. 10.5 shows this assumption appears reasonable. Only the final few points in the streamwise direction appear to be strongly influenced towards the base pressure.

10.2 Results and Discussions for $\alpha = -10.2^\circ$

The calculated surface streamlines for $Re_l = 3.0 \times 10^6$ when the entire surface is treated as turbulent show the boundary layer separates before the end of the model for $0^\circ \geq \varphi_e \geq -30^\circ$, contrary to the observed flow in Fig. 7.21 with a range of viscosity oils and thickness of application. The attachment of the flow in this region is, however, very sensitive to Reynolds number¹ as observed in Figs. 7.18, 7.19 7.21 and 7.22 and explained in Section 7.4. Fig. 10.6 shows the calculated surface streamlines using the realisable $k-\varepsilon$ turbulence model for a fully turbulent boundary layer overlaid on the corresponding flow visualisation. The calculated surface streamlines show a short open separation starting near $x_{bc}/l = 0.36$, $\varphi_e = -85^\circ$ that is not observed in the flow visualisation. The saddle on the flank at the start of the closed separation is located in a similar position to the one in the flow visualisation, though the angle of the flow leading to this saddle differs. The size of the calculated separated region is close to that observed in the flow visualisation. Overall, the agreement between the observed and calculated surface streamlines is good.

For this case at $Re_l = 3.0 \times 10^6$ when the measured laminar region was implemented, with the remaining region modelled using the realisable $k-\varepsilon$ turbulence model, the boundary layer on the pressure side separated upstream of the measured boundary layer transition region. The same behaviour was observed with the 3–1 spheroid at $Re_l = 2.5 \times 10^6$. In order to prevent this, the location of the transition region for $0^\circ \geq \varphi_e \geq -75^\circ$ was shifted upstream so $\bar{\gamma}_{0.25}$ was located at $x_{bc}/l = 0.36$, a maximum shift of $x_{bc}/l = 0.08$. With this change, the boundary layer avoids a laminar separation and stays attached on the pressure side for a slightly greater extent than when the entire surface is modelled as turbulent as shown by Fig. 10.7. However, a large open separation occurs on the flank in the laminar region starting near $x_{bc}/l = 0.12$, $\varphi_e = -95^\circ$; this open separation is not seen in the flow visualisation at $Re_l = 3.0 \times 10^6$. Upstream of the open separation there is close alignment between the calculated and observed

¹The boundary layer was seen to be attached until the end of the model at $Re_l = 2.0 \times 10^6$ (laminar separation bubble) and $Re_l = 3.0 \times 10^6$. It separated before the end of the model at $Re_l = 2.5 \times 10^6$ (laminar separation) and $Re_l = 4.0 \times 10^6$ (turbulent separation).

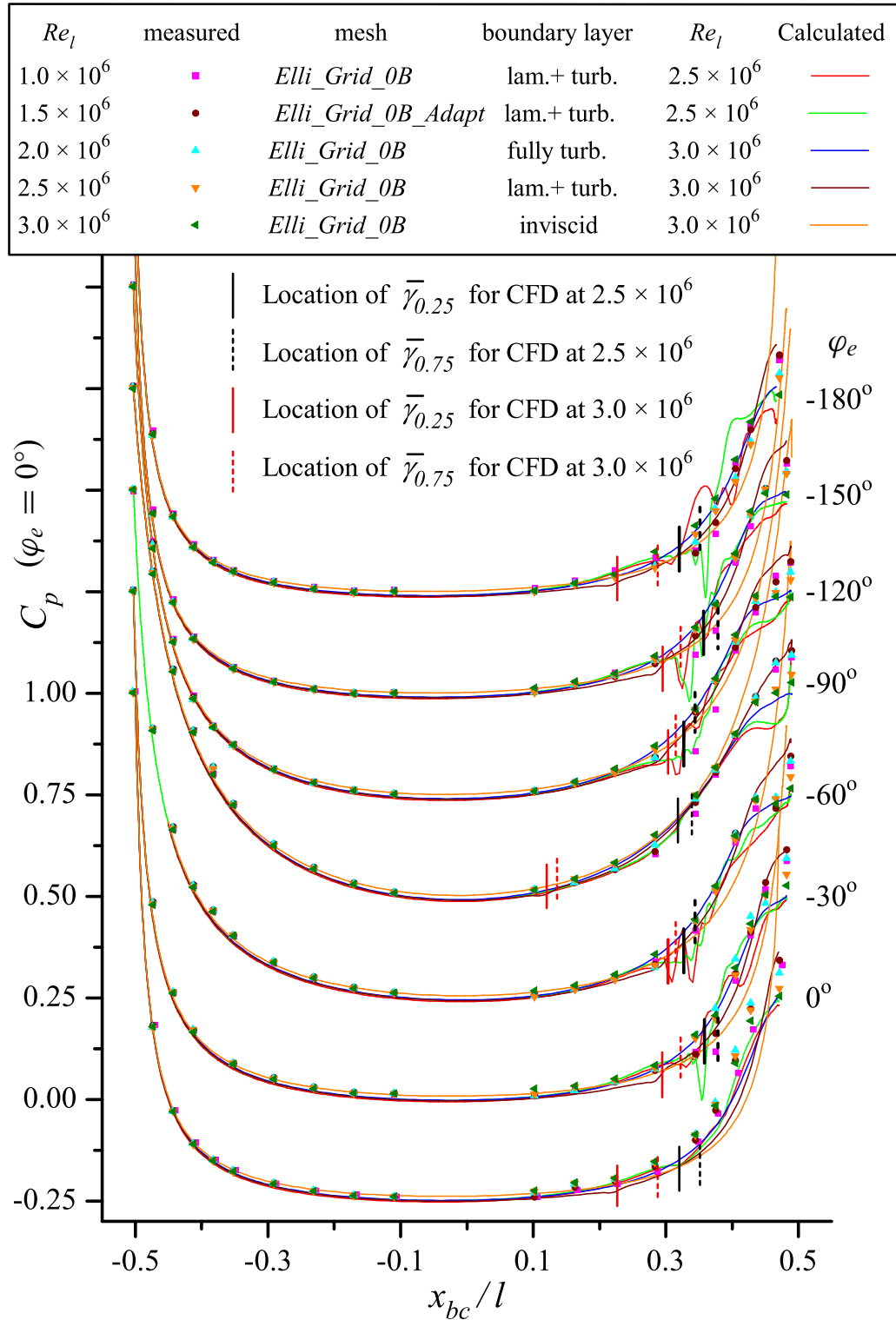


Figure 10.4: Computed and measured surface pressure distribution on ellipsoid, $\alpha = -0.2^\circ$, realisable $k-\varepsilon$ turbulence model. C_p values for each azimuth progressively displaced vertically by 0.25 for $\varphi_e < 0^\circ$. The computed results at $Re_l = 2.5 \times 10^6$ show laminar boundary layer separation upstream of the boundary layer transition zone.

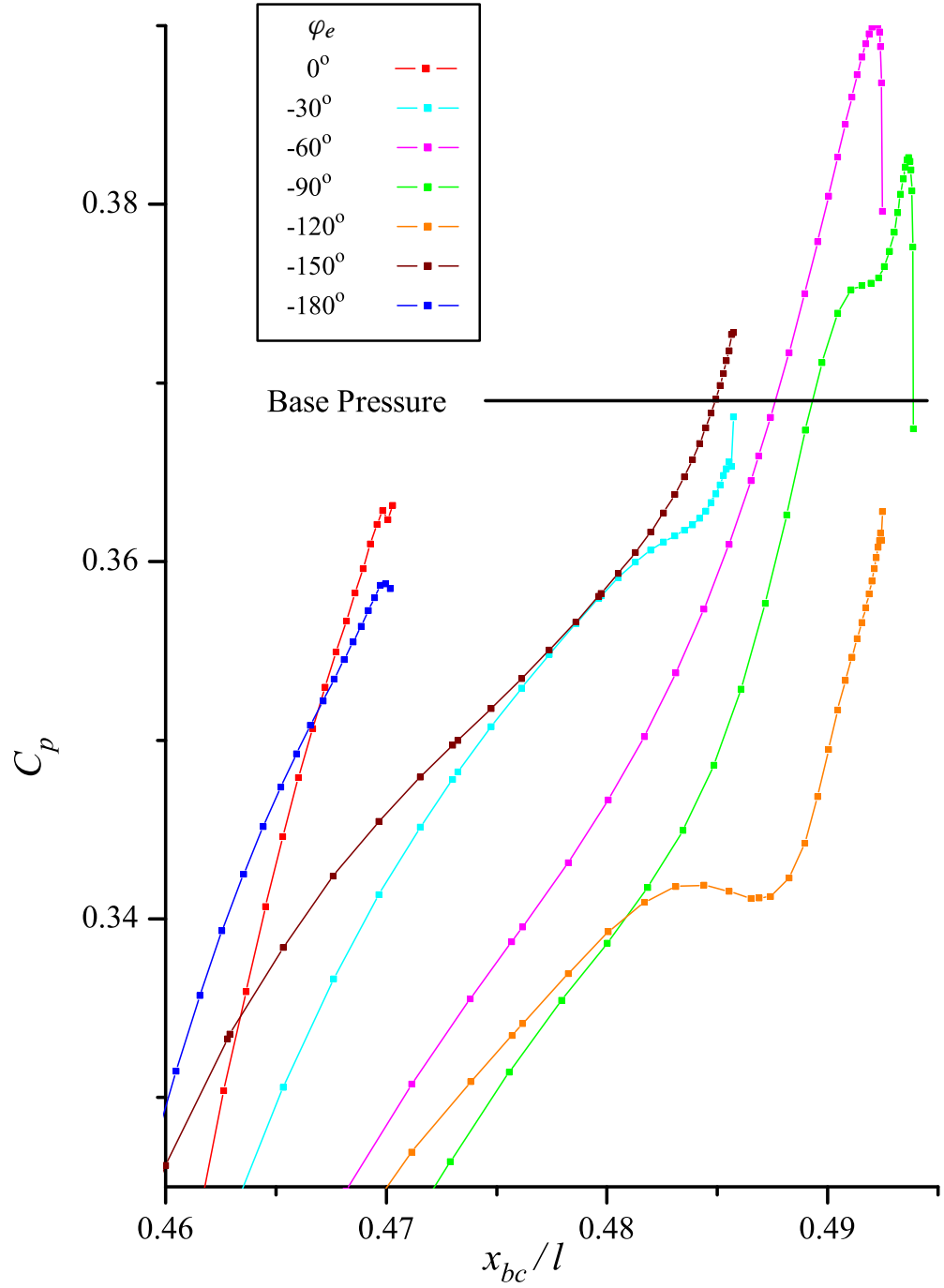


Figure 10.5: Computed surface pressure distribution near the rear of ellipsoid compared to the average internal pressure at $x_{bc} = 0.134\text{ mm}$, $\alpha = -0.2^\circ$ for $Re_l = 3.0 \times 10^6$ using the *Elli_Grid-10B* mesh using the realisable $k-\varepsilon$ turbulence model. The calculated base pressure appears to be a good approximation to the final on-surface calculated C_p .

surface streamlines. The open separation distorts the flow around the flank and the separated region at the rear of the flank.

Although the open separation on the flank calculated at $Re_l = 3.0 \times 10^6$ was not observed in the corresponding flow visualisation in Subsection 7.3.2, it was noted from the sequence of photos prior to Fig. 7.18 that at $Re_l = 2.0 \times 10^6$ the open separation extended further upstream. The position of the observed limiting surface streamline of the open separation, when it extended further upstream, coincides with that of the calculated open separation between its start near $x_{bc}/l = 0.0$, $\varphi_e = -105^\circ$ and $x_{bc}/l = 0.27$, $\varphi_e = -80^\circ$, where the observed limiting streamline ceases (Fig. 10.8).

The extent of calculated attached flow on the suction side with and without the laminar region implemented was similar and a good match to the observed surface streamlines; the limiting streamline occurred, around $x_{bc}/l = 0.45$ for $-120^\circ \geq \varphi_e \geq -180^\circ$. However, the observed surface streamlines show a greater divergence towards the flank than the computed surface streamlines. This difference may be attributed to the existence in the computed solutions of a node in the vicinity of $x_{bc}/l = 0.46$, $\varphi_e = -95^\circ$ where the surface streamlines leave the surface. A node in a similar position was not present in the flow visualisation; hence the surface streamlines diverged to the dominant foci on the pressure side of the flank separation in order to leave the surface.

A comparison of measured and computed surface pressure distributions for $Re_l = 3.0 \times 10^6$ show that at $\varphi_e = 0^\circ, -30^\circ, -150^\circ$ and -180° the computed result with the laminar region implemented provides a close match to the measured data. Closer to the flank the agreement is poorer. The significant difference between the computed result with and without laminar region at $\varphi_e = -90^\circ$ is accounted for by the presence of the much greater length of open separation in the former. The calculated result at $Re_l = 4.0 \times 10^6$ with the laminar region implemented has no open separation, and provides a good match to the measured result on the flank. It is also worth noting the greater variation in the measured pressure distribution for $Re_l \geq 1.5 \times 10^6$ when $-60^\circ \geq \varphi_e \geq -120^\circ$. This is consistent with the greater variation observed in the flow visualisation in this region.

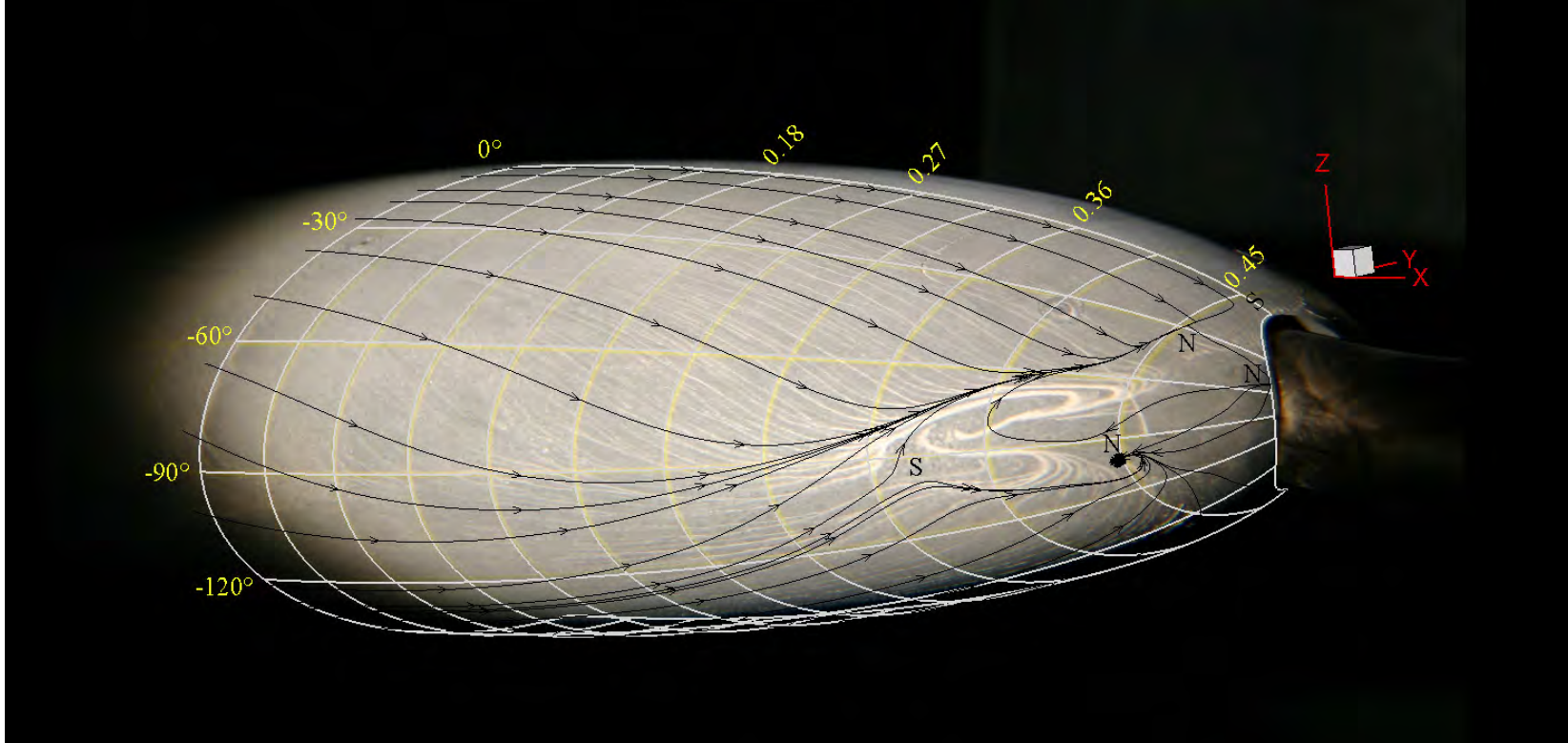


Figure 10.6: Computed surface streamlines on 4.2–2–1 ellipsoid using realisable $k-\varepsilon$ turbulence model with fully turbulent boundary layer overlaid on flow visualisation, $Re_l = 3.0 \times 10^6$, $\alpha = -10.2^\circ$, *Elli_Grid-10B*. A short open separation is calculated starting near $x_{bc}/l = 0.36$, $\varphi_e = -85^\circ$ and merging with the limiting streamline of the closed separation on the suction side near $x_{bc}/l = 0.39$, $\varphi_e = -70^\circ$. Calculated surface streamlines in black; white grid lines show mesh alignment. Calculated surface singularities marked in black

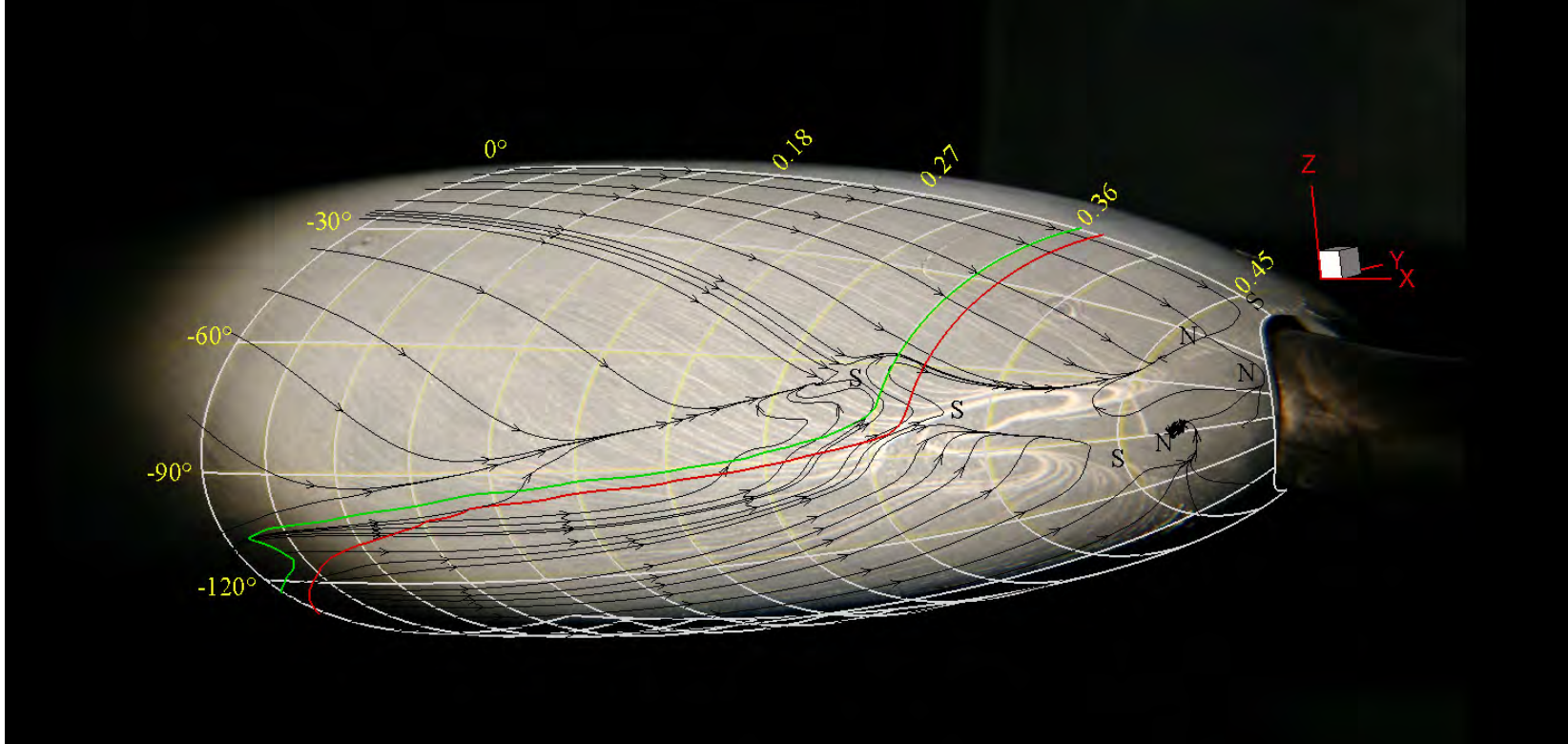


Figure 10.7: Computed surface streamlines on 4.2–2–1 ellipsoid using realisable k - ε turbulence model with the modified laminar region implemented overlaid on flow visualisation, $Re_l = 3.0 \times 10^6$, $\alpha = -10.2^\circ$, *Elli_Grid-10B*. A long open separation has been computed in the laminar region; this separation is not apparent in the flow visualisation. Calculated surface streamlines in black; white grid lines show mesh alignment. $\tilde{\gamma}_{0.25}$ and $\tilde{\gamma}_{0.75}$ contour shown in green and red respectively. Calculated surface singularities marked in black.

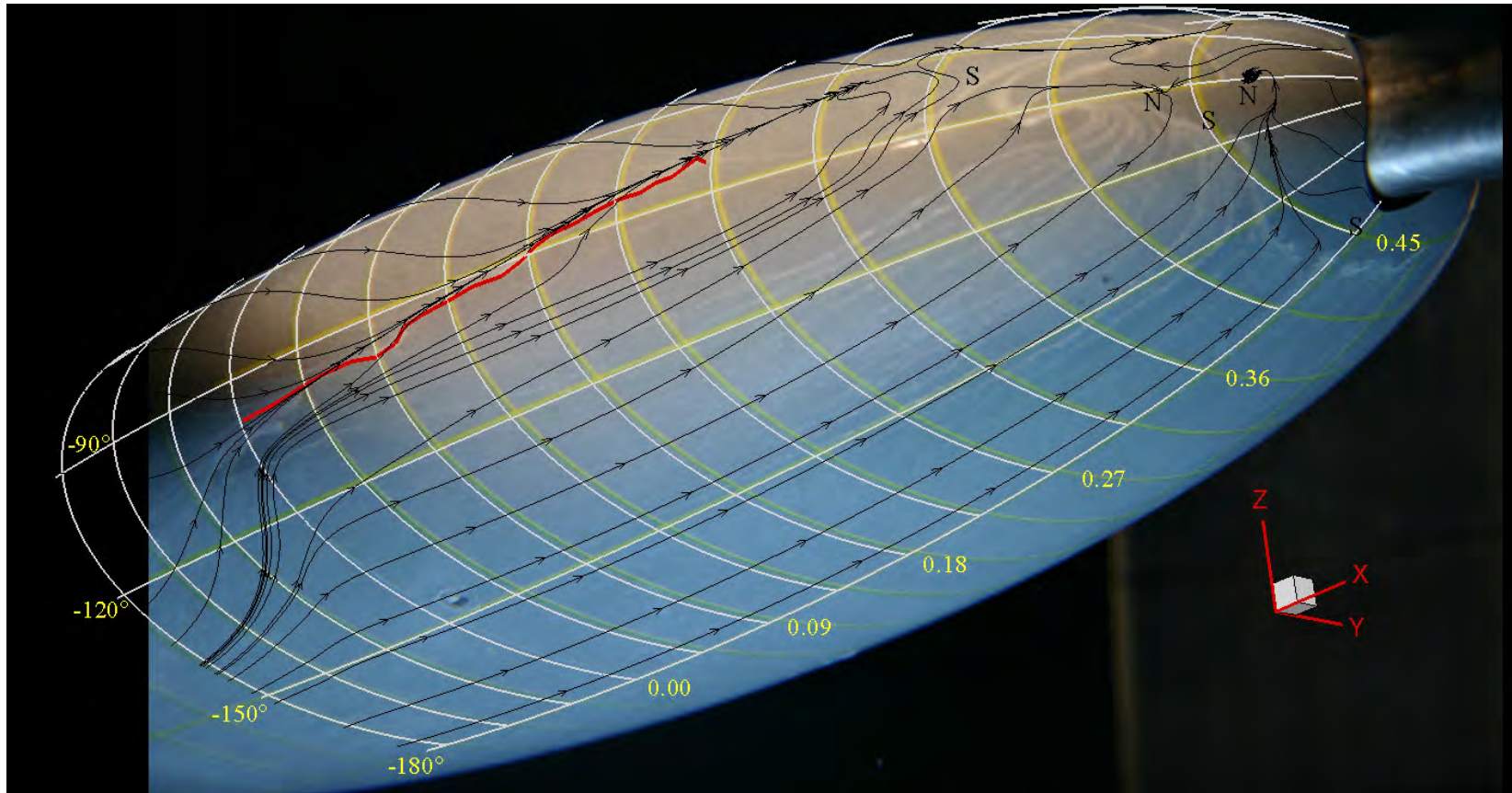


Figure 10.8: Computed surface streamlines on 4.2-2-1 ellipsoid using realisable $k-\varepsilon$ turbulence model with the modified laminar region implemented for $Re_l = 3.0 \times 10^6$, $\alpha = -10.2^\circ$, *Elli_Grid-10B* overlaid on flow visualisation at $Re_l = 2.0 \times 10^6$, $\alpha = -10.2^\circ$. The long open separation computed in the laminar region, at $Re_l = 3.0 \times 10^6$ coincides with one observed in some of the flow visualisation at $Re_l = 2.0 \times 10^6$. Calculated surface streamlines in black; white grid lines show mesh alignment, red line shows location of observed limiting streamline for the open separation.

10.3 Ellipsoid Wake Survey at $\alpha = -10.2^\circ$

The wake survey was carried out using the three-dimensional traverse and fast response total pressure probe (FRTTP) described in Chapter 8. The probe was used with a tip of 1.05 mm OD and 0.69 mm ID. The probe was aligned with the freestream flow and measurements were taken in a plane at $x_{bc}/l = 0.77$, 250 mm downstream of the ellipsoid centroid at $x_{bc} = 0$. When oriented into the flow the FRTTP measures the total pressure; the reference for this measurement (p_{ref}) is determined by the choice of connection for the reference port of the probe sensor. For these measurements the reference was taken on the tunnel wall in the measurement plane. The pressure measured by the probe is

$$p_{ftrtp} + p'_{ftrtp} = \frac{1}{2} \rho(u + u')^2 + (p - p_{ref}) + p' \quad (10.1)$$

where the ' designates the unsteady component. The length of tubing and the wet/dry interface acts as a low pass filter on the reference pressure.

A survey of a single plane consisted of 1216 measurement locations. Sampling occurred at 16384 Hz for 8 s at each position. As each survey took many hours the sensor drift was corrected by periodically comparing the FRTTP output when in the freestream. Corrections for the minor temporal changes in the freestream velocity were calculated from the pressure differential across the tunnel contraction. For $Re_l = 3.0 \times 10^6$ a contour plot of the output of the FRTTP normalised by the output in the freestream, $C_{p_{ftrtp}}$, is presented in Fig. 10.11(a). The surveys for $Re_l = 1.0 \times 10^6$ and $Re_l = 2.0 \times 10^6$ are available in Appendix G. Each measurement point is indicated by a white dot. These figures show three features:

- The dominant feature is near the $z_t = 0$ plane; at $Re_l = 1.0 \times 10^6$ and 2.0×10^6 it is a large circular structure centred near $y_t/l = 0.10$ (34 mm) that appears isolated from the sting. For $Re_l = 3.0 \times 10^6$ the centre of this structure has shifted to $y_t/l = 0.085$ (28 mm) and the shape of the structure has elongated in the z_t direction; the structure is now having a significant impact on the pressure distribution on the sting. The minimum $C_{p_{ftrtp}}$ is also relatively consistent with the values 0.50% , 0.44% and 0.47% for $Re_l = 1.0 \times 10^6$, 2.0×10^6 and 3.0×10^6 respectively. The decrease in $C_{p_{ftrtp}}$ at $Re_l = 2.0 \times 10^6$ may be explained by the open separation seen in the flow visualisation at this Reynolds number.
- The second structure has its minimum $C_{p_{ftrtp}}$ close to the sting; the position of this minimum shifts from near $\varphi = -30^\circ$ at $Re_l = 1.0 \times 10^6$ and 2.0×10^6 to -20° at $Re_l = 3.0 \times 10^6$.
- The third feature is the tongue of lower C_P , higher turbulence connecting the other two structures.

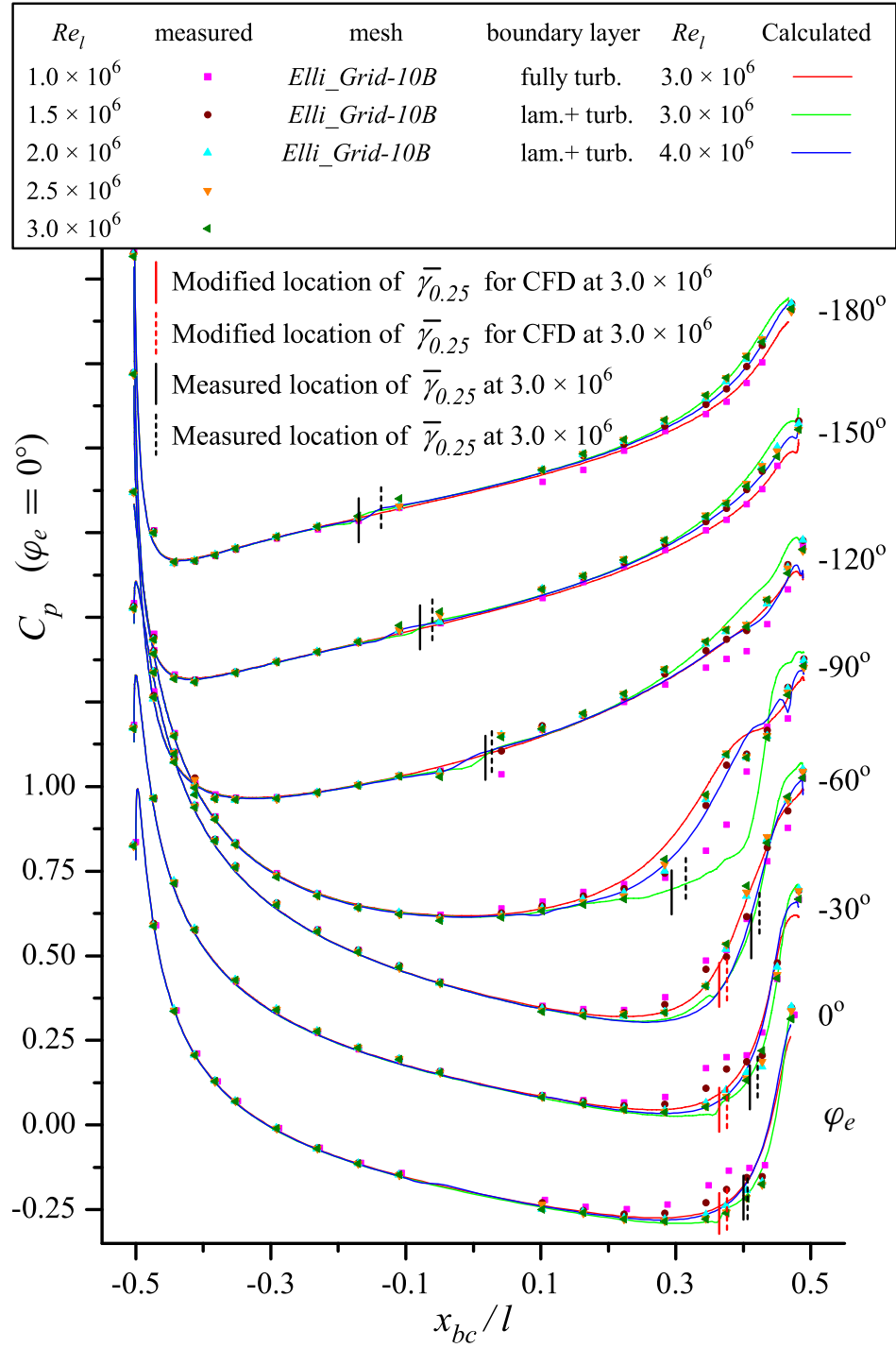


Figure 10.9: Computed and measured surface pressure distribution on ellipsoid, $\alpha = -10.2^\circ$, realisable $k-\varepsilon$ turbulence model. C_p values for each azimuth progressively displaced vertically by 0.35 for $\varphi_e < 0^\circ$. The calculations at $Re_l = 3.0 \times 10^6$ with the laminar region implemented show a marginally closer match to the measured data, including the base pressure measurement, except in the vicinity of the flank.

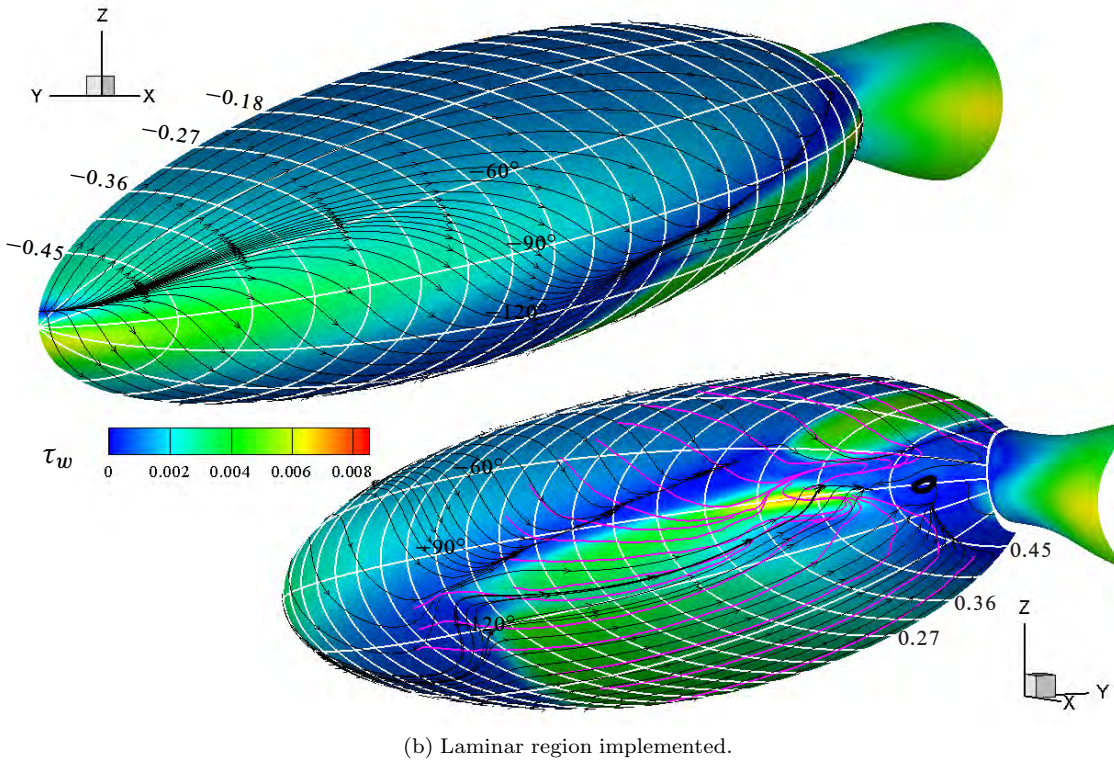
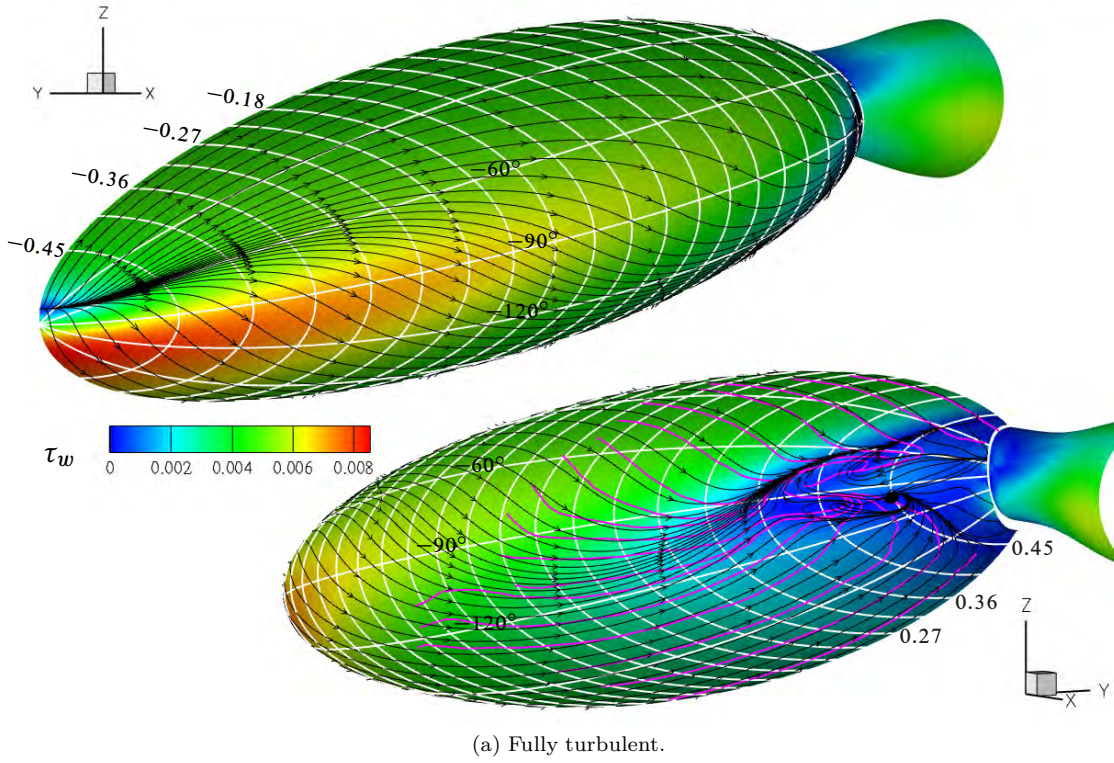


Figure 10.10: Computed surface streamlines on 4.2-2-1 ellipsoid using realisable $k-\epsilon$ turbulence model with and without laminar regions implemented, $Re_l = 3.0 \times 10^6$, $\alpha = -10.2^\circ$, *Elli_Grid-10B*. Surface streamlines from flow visualisation are shown in magenta, calculated surface streamlines in black.

The size of these three structures is much greater than the size of the probe tip.

If the contribution due to fluctuating pressure, p' , is neglected and the static pressure is known, the turbulence quantity $\sqrt{u'^2}/U_\infty$ may be calculated from Eq. 10.1. If the turbulence is assumed isotropic then,

$$\sqrt{u'^2}/U_\infty = \sqrt{2/3 k}/U_\infty \quad (10.2)$$

as $k = (1/2)(\overline{u'^2} + \overline{v'^2} + \overline{w'^2})$.

The calculations using the realisable k - ε turbulence model without laminar regions shows variation in the static pressure coefficient in the measurement plane. On the symmetry plane upstream of the support foil $C_{p_{frtpp}} = 0.26$, while in the centre of the main structure it decreases to -0.13 . Due to this variation it is not possible to accurately calculate u or u' without a measurement of the static pressure across this plane; this measurement was not performed.

A rough estimate, assuming a random distribution of fluctuations with a linear distribution of magnitude such that $\sqrt{u'^2}/U_\infty = 17\%$ when $C_{p_{frtpp}} = 0$, shows that using a $C_{p_{frtpp}} = 0$ instead of $C_{p_{frtpp}} = -0.13$ would result into an underestimate of the turbulence by 17%. Repeating the exercise using a $C_{p_{frtpp}} = 0$ instead of $C_{p_{frtpp}} = 0.26$ with $u'/u = 10\%$ shows an overestimate of $\sqrt{u'^2}/U_\infty$ by 17%. The nominal $\sqrt{u'^2}/U_\infty$ is presented in Fig. 10.11(b) with the acknowledgment of this error. The maximum nominal $\sqrt{u'^2}/U_\infty$ associated with the largest structure is relatively consistent, having values of 14%, 18% and 14% for $Re_l = 1.0 \times 10^6$, 2.0×10^6 and 3.0×10^6 respectively. The increase at $Re_l = 2.0 \times 10^6$ may be explained by the open separation seen in the flow visualisation at this Reynolds number.

The dominant wake structure extended beyond the hexahedral mesh surrounding the sting into the region using tetrahedral cells. In order to examine whether the additional numerical diffusion due to the tetrahedral cells was significant, an adapted version of grid *Elli_Grid-10B* was used to examine the computed wake and confirm grid independence at and upstream of the measurement plane. There was minimal difference between results from the original and the adapted mesh; the minimum non-dimensional total pressure, C_{p_T} , at the centre of the dominant structure in the plane of measurement differed by less than 0.01 and the maximum $\sqrt{u'^2}/U_\infty$ of this structure by less than 0.5%.

The results computed using the realisable k - ε turbulence model without laminar regions at $\alpha = -10.2^\circ$ for $Re_l = 3.0 \times 10^6$ are shown in Fig. 10.12. The computed C_{p_T} in the plane at $x_{bc}/l = 0.77$ shows a similar dominant structure as seen in the measured plane. The centre of the structure is positioned further away from the sting at $y_t/l = 0.103$ and is less elongated when compared to the measured result. The calculated minimum C_{p_T} at the centre of the dominant structure is 0.37, less than the measured C_{p_T} of 0.47 at this Re_l .

The calculated $\sqrt{u'^2}/U_\infty$ shows evidence of two structures; its maximum magnitude is approximately 70% of the measured nominal $\sqrt{u'^2}/U_\infty$. One of these structures is associated with the main structure observed in the contour plot of C_{p_T} . The second of these structures results from the boundary layer separation at the rear of the model. The calculated $\sqrt{u'^2}/U_\infty$ is significantly larger than the measured nominal $\sqrt{u'^2}/U_\infty$ observed in Fig. 10.11(b) at a similar location. The calculated turbulence in the second structure is produced at the interface of the slow moving fluid in the wake and the higher velocity fluid that has separated from the body on the pressure side. There is minimal streamwise vorticity associated with this second computed structure, as the flow is in the streamwise direction; thus it is not apparent in Fig. 10.13. If the non-streamwise components of vorticity are examined this structure is prominent. Given that the separation at the rear of the model in the measured case did not occur between $0^\circ \geq \varphi_e \geq -30^\circ$ before the end of the body,² it is reasonable that the magnitude of the turbulence in the tongue of lower pressure and higher turbulence fluid between the sting and dominant structure is much greater and more centred in the computed results. The greater magnitude of the turbulence of this structure masks the structure associated with the separation from the sting observed in the measured unsteady component (Fig. 10.11(b)).

The computational solution at $Re_l = 3.0 \times 10^6$ using the realisable $k-\varepsilon$ turbulence model without the laminar region implemented provided good agreement between the observed and calculated surface streamlines and the location of the separated region except, between $0^\circ \geq \varphi_e \geq -30^\circ$. The computed structures in the plane at $x_{bc}/l = 0.77$ also appear similar to those measured. Given this, an examination of the calculated flow structures upstream of the wake survey is useful in examining the origin of the structures observed in the wake survey. Fig. 10.13 shows contours of streamwise vorticity, Ω_{x_t} . Tracing the largest structure upstream from the plane at $x_{bc}/l = 0.77$ it is evident that development of this structure has already commenced at the most upstream section shown ($x_{bc}/l = 0.15$). The flow over the ellipsoid has a component in the azimuthal direction that produces streamwise vorticity within the boundary layer. As the surface streamlines converge, fluid is forced away from the surface. Once this fluid with increased streamwise vorticity is forced off the surface it is convected towards the suction side of the ellipsoid. The planes at $x_{bc}/l = 0.15, 0.23$, and 0.31 show the development of the dominant structure in the plane at $x_{bc}/l = 0.77$ prior to any boundary layer separation. The section at $x_{bc}/l = 0.38$ shows a continuation of the process described for the upstream locations though now the open separation has commenced. Downstream of the start of the closed separation two additional structures have formed. One has the same direction of rotation as the upstream structure; this originates near the foci where the surface streamlines from the suction side leave

²This flow is likely to reattach to the sting.

the surface and merge with the structure from upstream in the plane at $x_{bc}/l = 0.54$. This merging shifts the core of the dominant structure closer to the sting. The second structure from the closed separation has the opposite direction of rotation and develops from the fluid drawn into the region of recirculating flow on the pressure side. Between $x_{bc}/l = 0.54$ and $x_{bc}/l = 0.77$ this structure interacts destructively with the dominant structure and is no longer obvious by the time it reaches the measurement plane; it has, however, changed the shape of the dominant structure.

The lift generated by the ellipsoid imparts a vertical component to the flow in the wake. This crossflow on the sting results in another structure, visible near the sting in the plane at $x_{bc}/l = 0.77$.

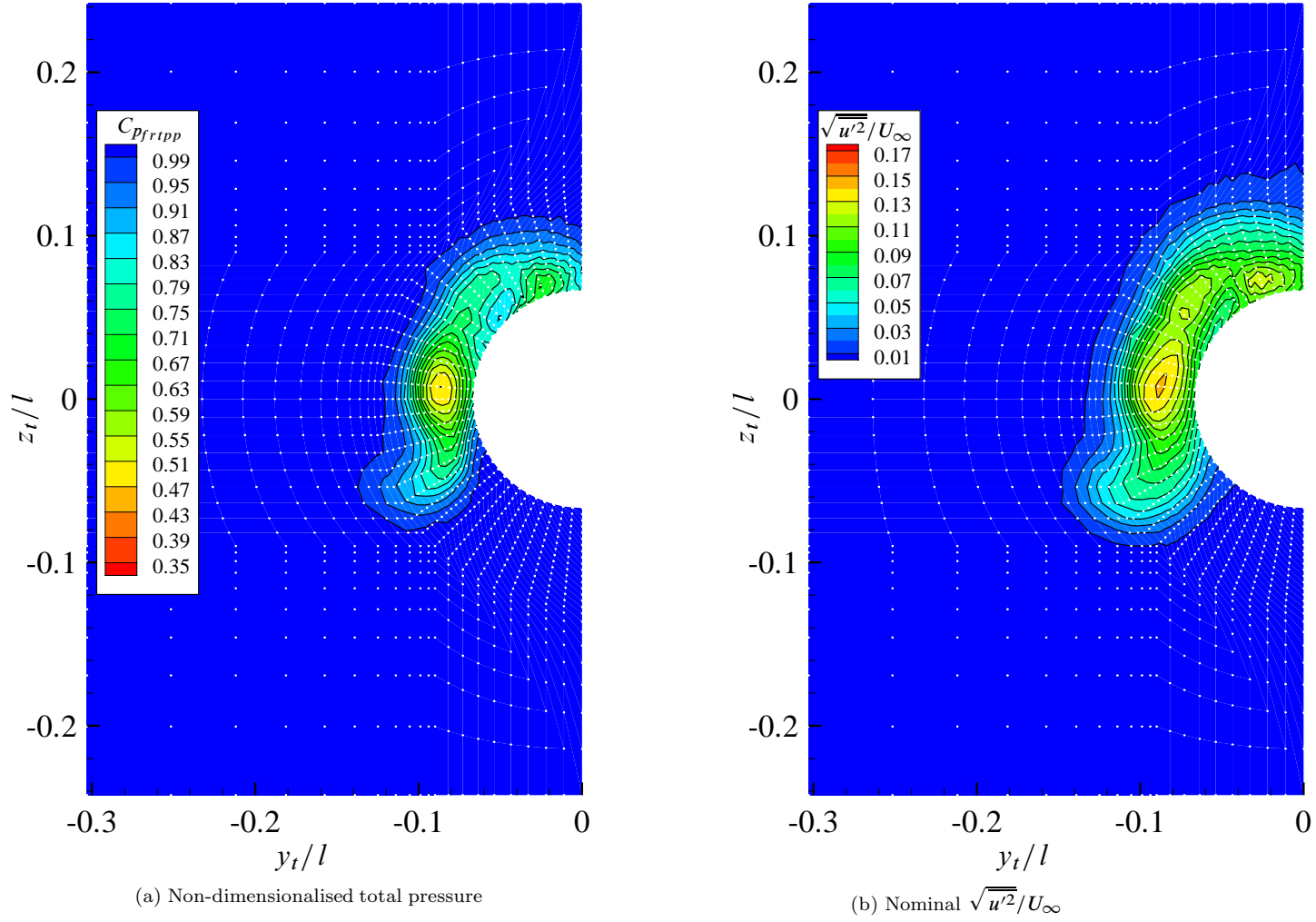


Figure 10.11: Wake measurements with the FRTPP in plane $x_t/l = 0.76$, 250mm downstream of ellipsoid centroid, $\alpha = -10.2^\circ$, $Re_l = 3.0 \times 10^6$.

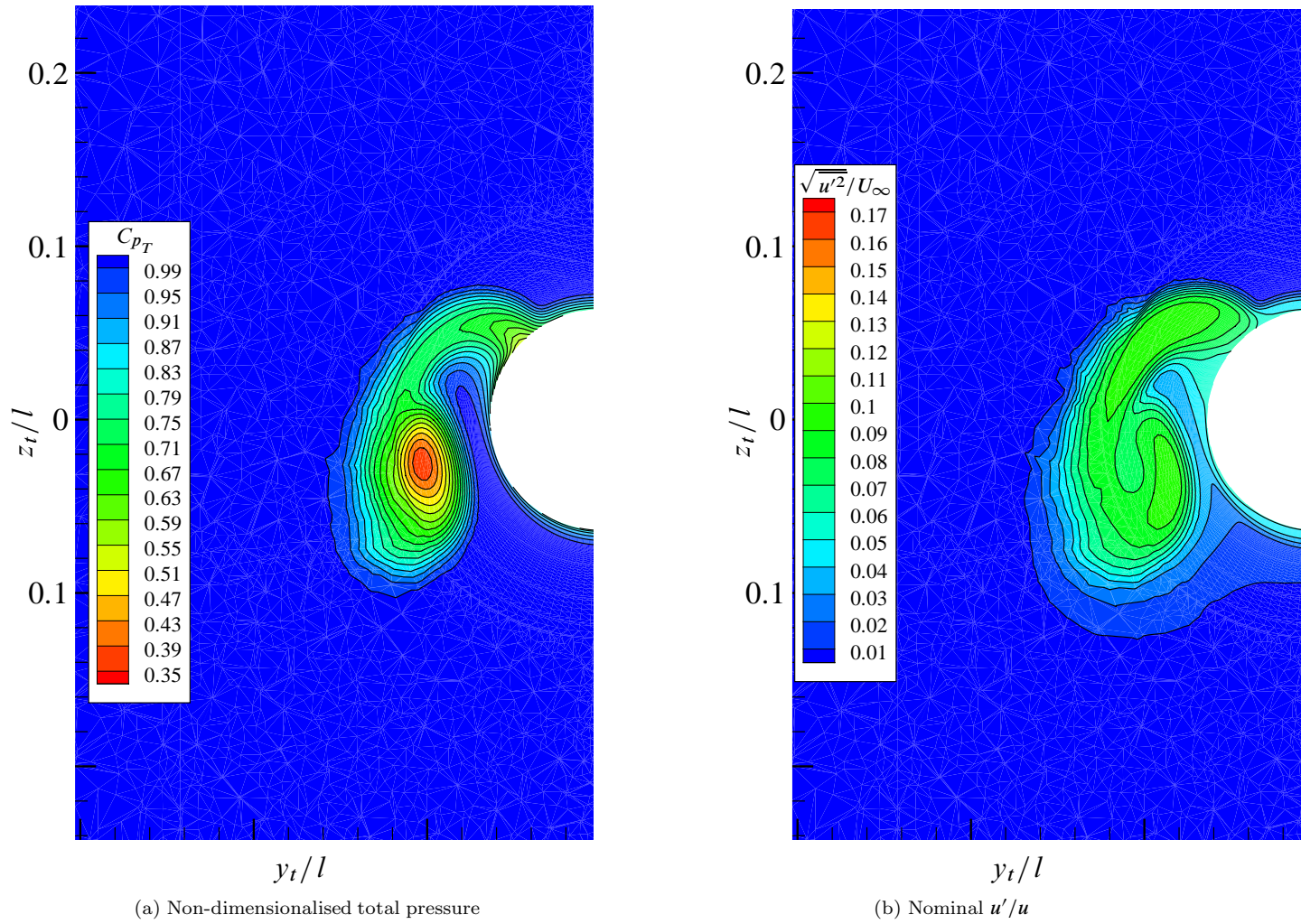


Figure 10.12: Calculated wake properties in plane $x_t/l = 0.76$, 250 mm downstream of ellipsoid centre, $\alpha = -10.2^\circ$, $Re_l = 3.0 \times 10^6$.

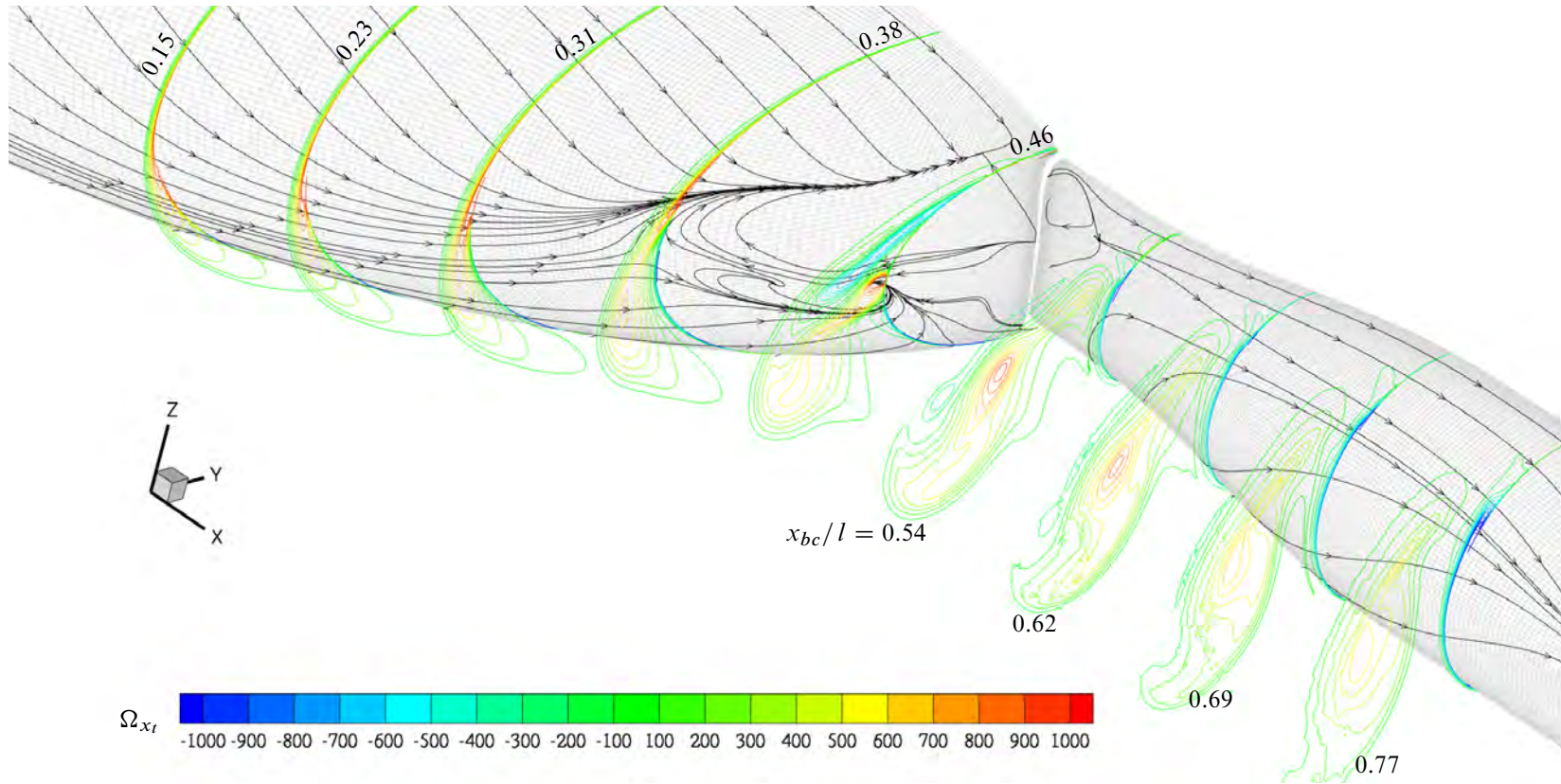


Figure 10.13: Computed contours of Ω_{x_i} for the 4.2–2–1 ellipsoid calculated using realisable k - ε turbulence model, $Re_l = 3.0 \times 10^6$, $\alpha = -10.2^\circ$, *Elli_Grid-10B_Adapt*. The dominate structure in the plane at $x_{bc}/l = 0.77$ has commenced development prior to any boundary layer separation. The new structure in the plane at $x_{bc}/l = 0.46$ that rotates in the opposite direction to the dominant structure interacts destructively with the dominant structure. Calculated surface streamlines in black.

10.4 Results and Discussions $\alpha = -10.2^\circ$, Boundary Layer Tripped

The main feature of interest for the ellipsoid with the largely turbulent boundary layer is that an open separation was observed in the flow visualisation (Fig. 7.16) on the flank between $x_{bc}/l = 0.2$, $\varphi_e = -105^\circ$ and $x_{bc}/l = 0.32$, $\alpha = -90^\circ$. Throughout these calculations there has been the problem that implementation of the boundary layer transition region has tended to lead to separation of the boundary layer. In this case, as boundary layer transition has occurred at $x_{bc}/l = -0.3$, it is possible to observe if the open separation is calculated without interference due to the implementation of the boundary layer transition region.

Fig. 10.14 shows a convergence of the computed surface streamlines on the flank towards the saddle of the closed separation at $x_{bc}/l = 0.38$, $\varphi_e = -100^\circ$. A short open separation is calculated starting near $x_{bc}/l = 0.36$, $\varphi_e = -85^\circ$ and merging with the limiting streamline of the closed separation on the pressure side near $x_{bc}/l = 0.39$, $\varphi_e = -70^\circ$; but no limiting streamline in the region of $x_{bc}/l = 0.2$, $\varphi_e = -105^\circ$ and $x_{bc}/l = 0.32$, $\alpha = -90^\circ$. The calculated saddle ($x_{bc}/l = 0.38$, $\varphi_e = -100^\circ$), is at a similar azimuth to the one observed in the flow visualisation ($x_{bc}/l = 0.32$, $\varphi_e = -100^\circ$) but further downstream. The dominant observed focus in the separated region on the flank ($x_{bc}/l = 0.39$, $\varphi_e = -80^\circ$) is not calculated. The node associated with the surface streamlines leaving the surface via the limiting streamline on the pressure side of this separation is calculated at $x_{bc}/l = 0.44$, $\varphi_e = -55^\circ$. This node is also connected to the limiting streamline of the separation on the pressure side for $0^\circ \leq \varphi_e \leq -50^\circ$. The location of this limiting streamline ($0^\circ \leq \varphi_e \leq -50^\circ$) coincides with the observed location of separation. The position of the calculated foci at the end of the limiting streamline on the suction side of the closed separation also coincides with the observed foci.

The calculated and measured surface pressure distributions show good agreement except in regard to three factors. As seen previously the positive shift in C_p downstream of boundary layer transition is not apparent in the calculations. On the flank the measured pressure distributions show a greater perturbation in the region where the limiting streamline of the open separation joins the limiting streamline on the pressure side of the closed separation (Fig. 7.16). The calculated C_p near the rear of the model is slightly less on the pressure side and slightly greater on the suction side when compared to the measured data. There is good agreement between the measured and calculated base pressures.

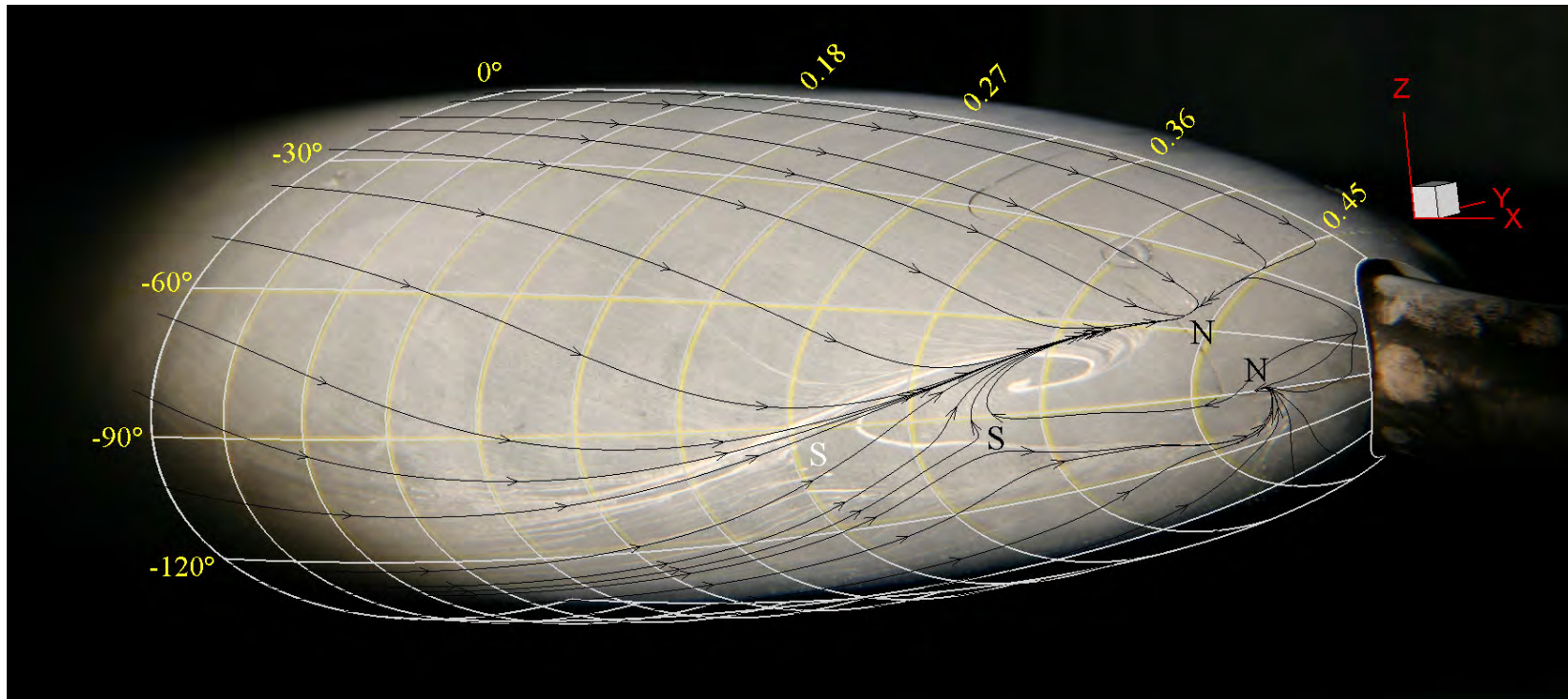


Figure 10.14: Computed surface streamlines on 4.2–2–1 ellipsoid using realisable $k-\varepsilon$ turbulence model with boundary layer transition forced at $x_{bc}/l = -0.3$, overlaid on flow visualisation, $Re_l = 3.0 \times 10^6$, $\alpha = -10.2^\circ$, *Elli_Grid-10B*. A short open separation is calculated starting near $x_{bc}/l = 0.36$, $\varphi_e = -85^\circ$ and merging with the limiting streamline of the closed separation on the suction side near $x_{bc}/l = 0.49$, $\varphi_e = -70^\circ$. Calculated surface streamlines in black; white grid lines show mesh alignment. Calculated surface singularities marked in black; those observed in white.

10.5 Force and Moment Calculations

Without the implementation of laminar regions the influence of surface shear stress will be over calculated, as evident in the figures displaying the surface shear stress in this and the preceding chapter. The influence of surface shear stress is most obvious at zero incidence as the component of form drag due to lift (induced drag) is absent. The following discussion uses the calculated results obtained with the realisable k - ε turbulence model. For the fully turbulent case the calculated drag due to surface shear stress is 86% of the total drag at $Re_l = 3.0 \times 10^6$. Table 10.2 shows that the increased shear stress with no laminar region implemented results in a calculated form drag more than double that of the corresponding case with the laminar region implemented. Even with the laminar region implemented the calculated drag is greater than measured. It is convenient to attribute the greater calculated drag to boundary layer separation between $0^\circ \leq \varphi_e \leq -30^\circ$ and $-150^\circ \leq \varphi_e \leq -180^\circ$ in the computed case, as the flow was attached at the end of the body for these azimuths in the flow visualisation. However, Fig. 10.4 shows greater pressure recovery for the calculated case (with the laminar region implemented) than the measured case. This would result in a reduction in the calculated drag. The measured drag for the ellipsoid at $Re_l = 3.0 \times 10^6$ appears small, so a more detailed examination is provided. The measured values of C_D at $Re_l = 2.0 \times 10^6$ and $Re_l = 3.75 \times 10^6$ are 0.0115 and 0.0128 respectively. The measured values approaching $Re_l = 3.0 \times 10^6$ from both directions are consistent, so these readings are in a region of minimum drag typical of transcritical conditions.

It is worth examining the computed values of drag for the 3–1 spheroid. A figure (Chapter 3, fig. 19) in Hoerner [53] shows a C_D of ≈ 0.05 for a 3–1 spheroid in supercritical flow ($Re_l \approx 10^6$). This value compares well with the calculated C_D for the 3–1 spheroid at zero incidence without laminar regions implemented at $Re_l = 2.0 \times 10^6$ of 0.0505 (81% of which is due to surface shear stress). When the laminar region for this incidence is implemented, with the slight modification to make the transition region axisymmetric, the calculated C_D is 0.019 (59% due to surface shear stress). This calculation in transcritical conditions results in a C_D that is 38% of that in the supercritical condition. Based on these calculations it appears that despite the slightly greater wetted area (8%) of the 4.2–2–1 ellipsoid when the laminar region on each body is implemented the 4.2–2–1 ellipsoid has a lower C_D than the 3–1 ellipsoid for a Reynolds number around $Re_l = 3.0 \times 10^6$. This is reasonable as the 4.2–2–1 ellipsoid is less bluff and the increased wetted area has less influence when the majority of the surface has a laminar boundary layer. Dress [109] also notes that the drag coefficient can be reduced by the presence of a sting, as it acts as an extension of the body increasing the fineness ratio and/or by “breaking up” the separated wake region. In summary, the small value of the calculated C_D with the laminar

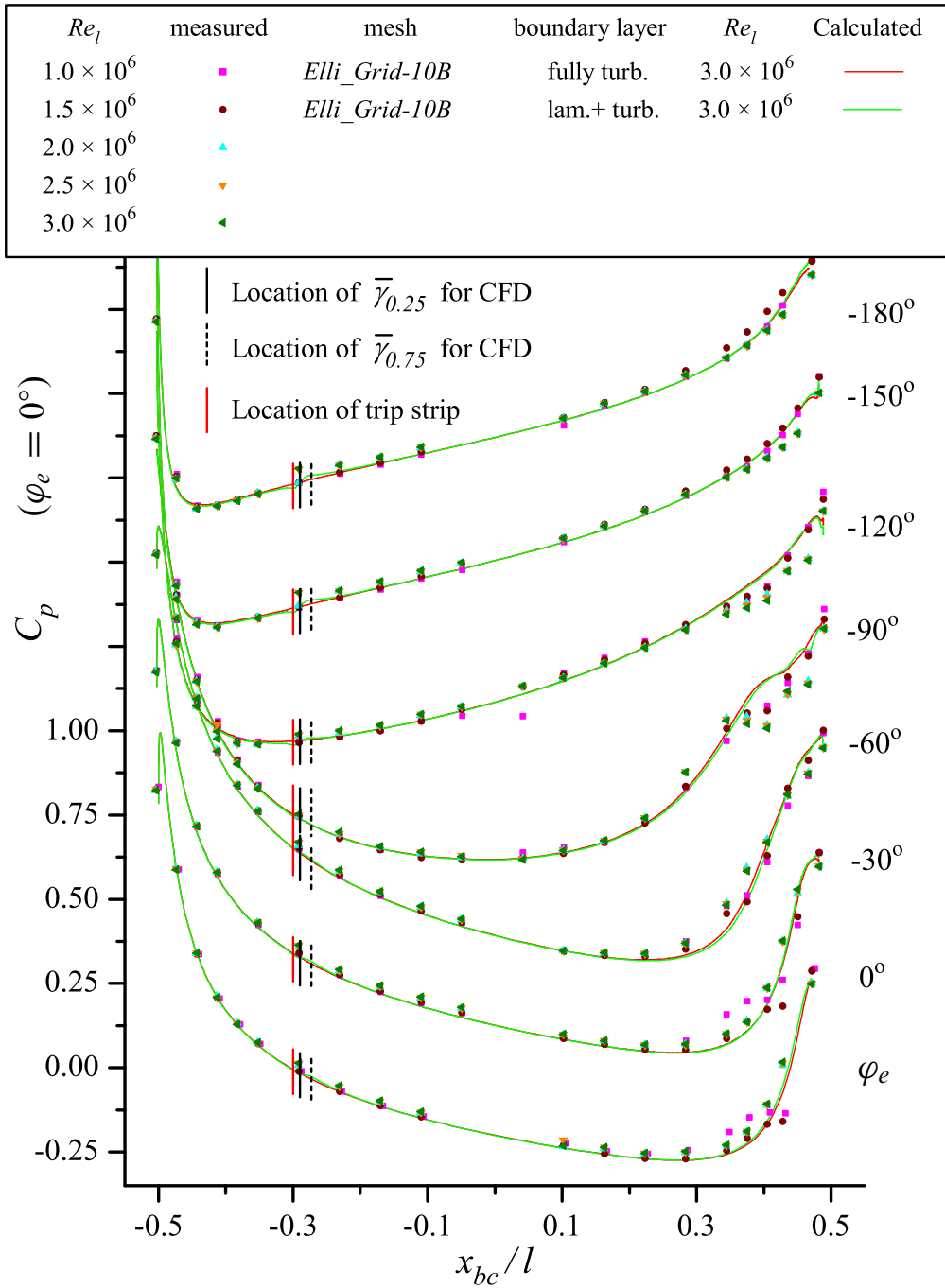


Figure 10.15: Computed and measured surface pressure distribution on ellipsoid with trip strip placed at $x_{bc}/l = -0.3$, $\alpha = -10.2^\circ$, realisable $k-\varepsilon$ turbulence model. C_p values for each azimuth progressively displaced vertically by 0.35 for $\varphi_e < 0^\circ$. The agreement between the measured and computed results is adversely influenced by the failure to calculate closed flank separation further upstream, as observed in the flow visualisation and indicated by the surface pressure distribution.

	form	viscous	total
Fully Turbulent	0.00646	0.04115	0.04760
Laminar + Turbulent	0.00211	0.01249	0.01460
Measured	0.0093 ± 0.0030		

Table 10.2: Calculated C_D using realisable k - ε turbulence model and measured drag for 4.2-2-1 ellipsoid at -0.2° incidence for $Re_l = 3.0 \times 10^6$.

region appears reasonable; but the difference between the measured and calculated value is not explained so far.

The following discussion continues to use the calculation with the laminar region implemented for $Re_l = 3.0 \times 10^6$. Examination of the calculated form drag shows it is very sensitive to the size of the opening for the sting. The calculated form drag on the front and rear half of the model is 0.2153 and -0.2132 respectively resulting in a total form drag of 0.0021. Enlarging the hole by 0.21% of $A_{x_{bc}}$ (or by 0.1 mm all round) increases the total drag by approximately 9%. The calculated drag is also sensitive to the state of the boundary layer. The boundary layer over the front half of the model is laminar and the viscous shear stress over this half contributes 51% of the total drag. The turbulent boundary layer on the rear half where the boundary layer has not separated occupies 29% of the surface area normal to the freestream flow direction of the rear half, and contributes 59% of the viscous drag for this half. In terms of the total drag this region with a turbulent boundary layer contributes 21%. As the position of boundary layer transition is sensitive this is another source of possible error in the comparison between measured and calculated drag. Given the sensitivity of both measurement and calculation, combined with the earlier separation of the boundary layer between $0^\circ \leq \varphi_e \leq -30^\circ$ and $-150^\circ \leq \varphi_e \leq -180^\circ$ in the computed case, the agreement for C_D shown in Table 10.2 is satisfactory.

This drag calculation at zero and low incidence is important if range, top speed, and the ocean currents an Unmanned Underwater Vehicle is able to operate in are to be determined. This calculation is therefore of interest despite the inherent difficulties and errors involved.

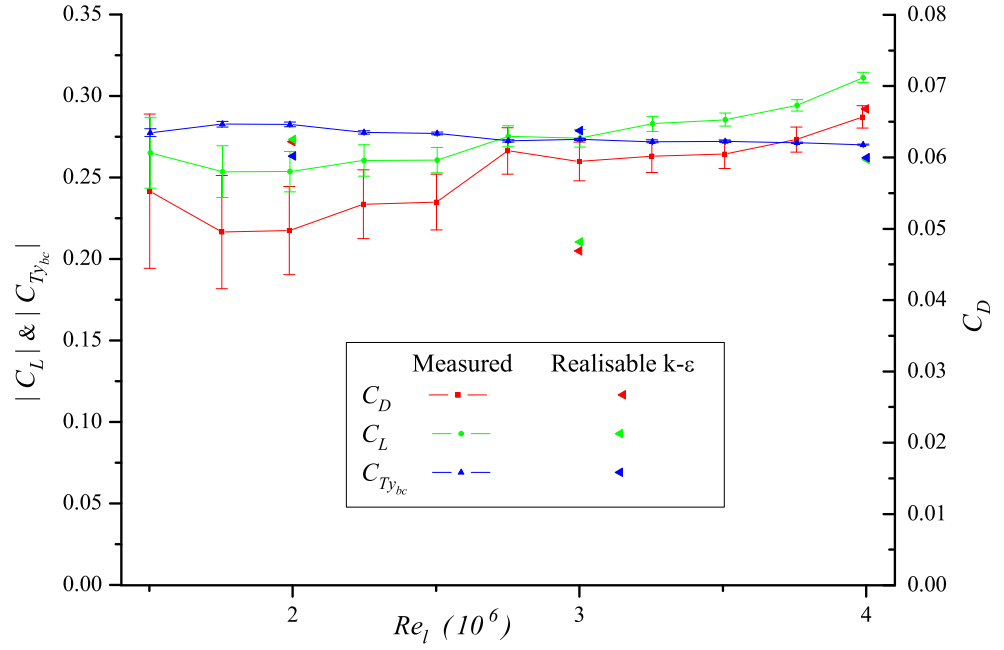
At an incidence of -10.2° there was less than 1.3% difference between the lift or moment calculated on the coarsest and finest meshes listed in Table 10.1 using the realisable k - ε turbulence model without laminar regions implemented. The calculated and measured loads are compared in Fig. 10.16. For $\alpha = -10.2^\circ$ using the realisable k - ε turbulence model with the measured or slightly modified boundary layer transition region implemented at $Re_l = 2.0 \times 10^6$ and 3.0×10^6 an open separation was calculated. At $Re_l = 2.0 \times 10^6$ the calculated open separation was longer than the one observed in the flow visualisation. For $Re_l = 3.0 \times 10^6$ no

open separation was present in the flow visualisation. Downstream of the open separation on the pressure side an area of separated boundary layer was present in the calculated result at $Re_l = 2.0 \times 10^6$ and 3.0×10^6 . This area is notably larger at $Re_l = 2.0 \times 10^6$. No separation was apparent in this region in the corresponding flow visualisation. As such agreement between measured and calculated loads is expected to be poor for this Re_l range, the result is not further examined. At $Re_l = 4.0 \times 10^6$ the calculated C_D and $C_{T_{ybc}}$ are close to the measured values. The calculated $|C_L|$ is 17% less than the measured value. This trend of under predicting $|C_L|$ also occurred with the spheroid and ellipsoid when the boundary layer was tripped.

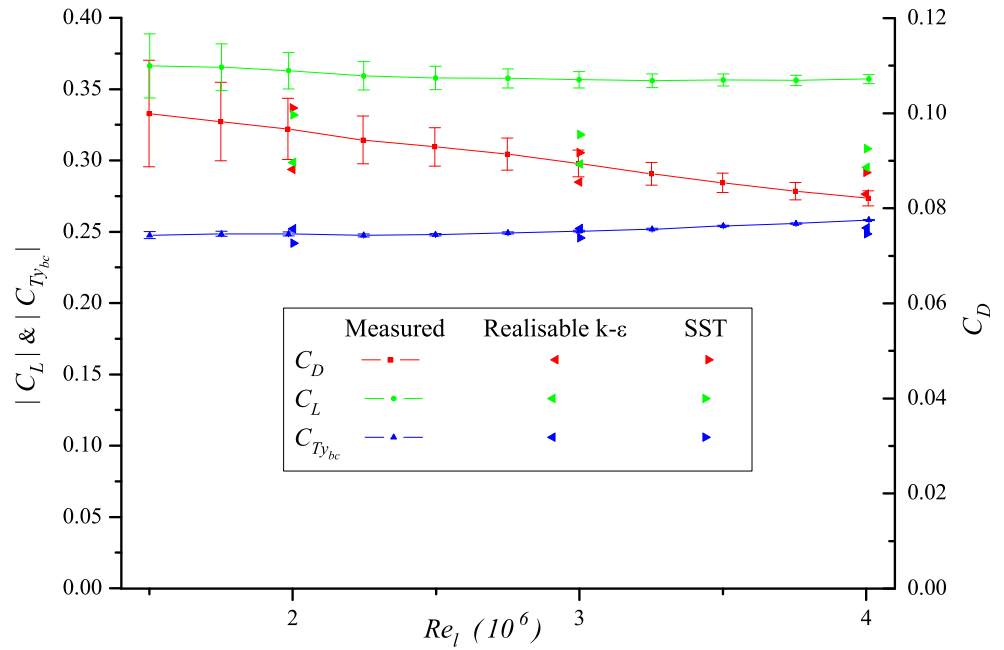
For the calculations with boundary layer transition set at the location of the trip strip for $\alpha = -10.2^\circ$ both the realisable $k-\varepsilon$ and SST turbulence models were used. The results for the loads using these two turbulence models were similar at $Re_l = 4.0 \times 10^6$, but showed greater variation at the lower Reynolds numbers. The calculated C_D with the boundary layer transition is close to the measured value when the trip strip was employed. The magnitude of the calculated C_L is in the order of 15% smaller than the measured result for the corresponding case. The cause of this is apparent in the comparison between measured and calculated C_p distributions shown in Fig. 10.15. On the suction side (near $\varphi = -150^\circ$) at the rear of the body the measured C_p is less than that calculated, whereas on the pressure side the measured values are greater than calculated (for the range of Re_l where the trip strip is effective). The influence of this difference in pressure is not apparent in the calculations of $C_{T_{ybc}}$ due to the dominant Munk moment. There is little difference between measured and calculated $C_{T_{ybc}}$. Although the agreement between measured and calculated C_D appears favourable, the calculated C_D is expected to increase if the calculated C_L were closer to the measured C_L .

10.6 Summary

For the ellipsoid calculations presented in detail with $Re_l = 3.0 \times 10^6$ the boundary layer at the rear showed premature separation near the vertical symmetry plane. This premature separation occurred for $\alpha = -0.2^\circ$ and on the pressure side for $\alpha = -10.2^\circ$; it occurred with and without the implementation of the measured (or slightly modified) laminar region. The only case where premature boundary layer separation was not calculated was when the boundary layer was tripped. In this case the measured boundary layer separated prior to the end of the model. For the other cases flow visualisation showed the boundary layer attached at the end of the model near the vertical symmetry plane. This early separation at $\alpha = -10.2^\circ$ leads to increased turbulence in the calculated wake. At $\alpha = -0.2^\circ$ when the laminar region was implemented the calculated surface streamlines on the flank for $Re_l = 3.0 \times 10^6$ matched those observed in the flow visualisation. At $\alpha = -10.2^\circ$ without the laminar region implemented the calculated



(a) Natural transition



(b) Forced transition

Figure 10.16: Comparison of measured and calculated loads, $\alpha = -10.2^\circ$. Due to the sensitive nature of natural boundary layer transition, variation between the measured and calculated loads is expected. The difference between the measure and calculated C_L in the case with the natural transition is consistent with pressure distributions in Fig. 10.15.

surface streamlines are similar to those observed at $Re_l = 3.0 \times 10^6$, except for the region near the vertical symmetry plane and a short open separation. When the laminar region was implemented, at this incidence and Reynolds number, a long open separation was computed that was not observed in the flow visualisation. However, a large part of this computed open separation aligned with one observed at $Re_l = 2.0 \times 10^6$, and a similar open separation was observed at $\alpha = -10.2^\circ$, $Re_l = 2.5 \times 10^6$ (Figs. 7.24 and 7.25). The surface pressure distributions measured on the flank at $Re_l = 3.0 \times 10^6$ were similar to those calculated at $Re_l = 4.0 \times 10^6$ with a laminar region implemented. These glimmers of improvement show the potential in allowing for the laminar regions if the premature laminar separations can be avoided. It may be unrealistic to expect a match between measured and calculated values and flow features for each Reynolds number; however, calculating the trends and the development of features appears possible.

A comparison of the measured and computed wake showed the increase in turbulence due to the calculation of the separation near the symmetry plane. Despite this difference the computed result is useful in examining the origin of the dominant structure in the measurement plane and its possible interactions with other flow structures. At the rear of the ellipsoid and spheroid near the horizontal symmetry plane of the model significant structures have been observed in surface flow visualisation when the model is at incidence. Fig. 10.13 shows that disturbance to the flow near this location extends a significant distance away from the model. A control surface placed in this location would experience complex flows when the model was at incidence: boundary layer separation near the root and the influence of the dominant vortical structure from the body closer to the tip. A UAV built by the National Taiwan University [10] has control surfaces at the rear of the body on the horizontal symmetry plane.

The calculated drag and lift with the forced boundary layer transition compare reasonably well with the measurement. When no trip strip was employed the match was poorer, as expected, given difficulties with the implementation of the boundary layer and the sensitivity of both measurement and calculation. The calculations also provide an insight into the possible direct contributions of surface pressure and wall shear stress to the total force on the body, along with the sensitivity of comparing measured and computed results.

Chapter 11

Conclusion

The role of unmanned vehicles has increased dramatically over the last decade, both in maritime and aeronautical operations. The motivations behind this include the desire to minimise exposure of people to hazardous environments; the savings in mass, space and cost that can be achieved when life support equipment is not required; and the desire to exploit resources in increasingly difficult locations. UUVs currently play a key role in mine hunting operations for many navies and in the offshore petroleum industry. A significant niche appears likely for UUVs deployed from submarines. In this role they can conduct operations in more difficult locations with less risk, and consequence, of exposure.

Many of these unmanned vehicles are considerably smaller and operate at lower speeds than more traditional manned platforms; as such they operate at lower Reynolds numbers. The hull shape of UUVs also often departs from the circular cross-section (ignoring any casing) seen on most traditional submarines.

A significant body of work exists examining the flow around prolate spheroids experimentally and computationally. A large proportion of that work has been with the finer 6–1 prolate spheroid with a focus on application to submarines; much of it has been performed at high angles of incidence and specifically examined crossflow separation. There are few studies into the flow around bluffer spheroids; less again in the transcritical Reynolds number range. There are minimal studies of the flow about scalene ellipsoids at any range of Reynolds number or incidence.

The present research into the flow about two low aspect ratio ellipsoids was primarily aimed at providing insight into the flow about these bluffer generic hull shapes. This study has been performed at incidences ranging from zero through to moderate angles in transcritical flow conditions. These flow conditions are relevant to the operation of streamlined UUVs.

The knowledge gained in the experimental part of this research is valuable for assessing the

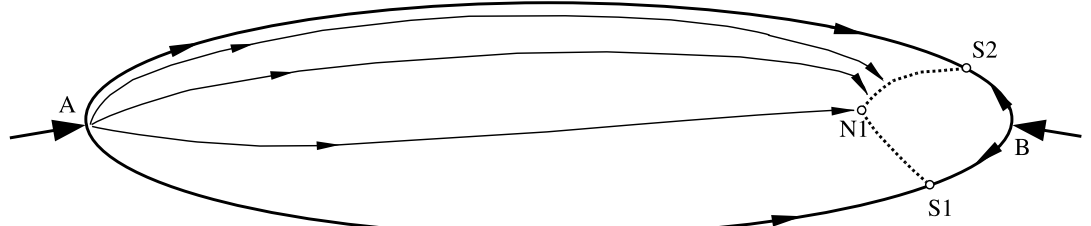
ability of CFD codes to calculate the complex flow that exists about these bodies. The second aim of this study was to examine the performance of a commercial CFD code using two-equation turbulence models. These models were modified to allow for laminar boundary layer regions. The numerical work in-turn assists the interpretation of flow features and measurements.

The major flow feature on the 3–1 spheroid and the 4.2–2–1 ellipsoid at low to moderate incidence (5° to 10°) was found to be a closed flank separation. This occurred at the rear of the spheroid where boundary layer separation occurred on both the suction and pressure side symmetry plane upstream of the base of the model. For the 4.2–2–1 ellipsoid the rear flank separation tended to be the dominant feature even if flow separation on the symmetry plane did not occur upstream of the end of the model. For the ellipsoid at lower Reynolds numbers this closed flank separation at the rear of the model was in some cases preceded by an open separation.

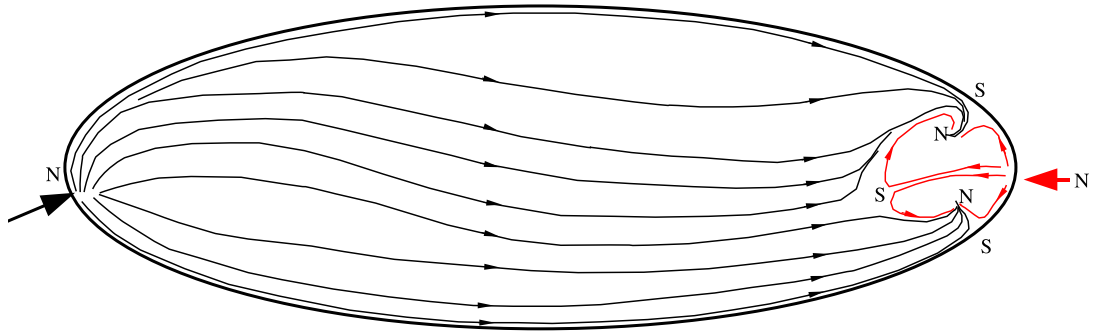
The rear flank separation is obvious in the flow visualisation; it is also apparent in the local flattening of surface pressure distribution curves (Fig. 4.11(a) and 5.14(c)) in this region; and it is predicted in the computational results (Fig. 9.30). This flank separation is also reported by Han and Patel [15]. In their studies on a 4.3–1 prolate spheroid in laminar flow ($Re_l = 8 \times 10^4$) at low to moderate incidences they report a similar flank separation when boundary layer separation occurs on the suction and pressure side of the symmetry plane upstream of the end of the model.

One significant difference, however, is that Han and Patel's sketch of the surface stream line topology, shown in Fig. 11.1(a), shows a node at the most upstream singularity on the flank. The surface streamline topology for the flank separation observed for the spheroid and ellipsoid at low to moderate incidence in this thesis showed a saddle at this location. The most common surface streamline topology observed in this work had two additional nodes of separation at the junction of the separation lines from the saddles on the pressure and suction side symmetry plane and the separation lines from saddle on the flank. This topology is consistent with the requirement that the number of nodes exceed the number of saddles by two and is shown in Fig. 11.1(b). Additional saddles and nodes were observed in some of the flow visualisation photos (Fig. 7.16).

Han and Patel's results show an open separation for the 4.3–1 prolate spheroid at an incidence of 10° . No such open separation was seen for the 3–1 spheroid in the results presented in this work. This difference, however, can be attributed to the greater Reynolds numbers investigated in these tests and the models' bluffer form. Open separations were observed on the flank of the 4.2–2–1 ellipsoid at incidence for $Re_l = 2.0 \times 10^6$, but not at $Re_l \geq 3.0 \times 10^6$. In their discussion of this open separation Han and Patel [15] provide a detailed discussion on



(a) Topology suggested by Han and Patel for a 4.3–1 spheroid at $\alpha = 5^\circ$, $Re_l = 8 \times 10^4$, dotted line closed separation. (see Han and Patel [15] Figure 6 (b))



(b) Common topology of dominant singularities observed for the 3–1 spheroid and 4.2–2–1 ellipsoid at low to moderate incidence in Chapter 7.

Figure 11.1: Topology of singularities in surface streamlines.

the influence of the azimuthal pressure gradient. Their explanation of how the large azimuthal pressure gradient in the boundary layer prevents a convergence of the surface streamlines on the suction side of the spheroid is relevant to the extended length of attached flow observed in the present work on the suction side of the spheroid and ellipsoid at incidence.

Another factor contributing to this extended length of attached flow on the suction side symmetry plane has been identified in the present study. The CFD results show how a small azimuthal pressure gradient in a region of relatively thick boundary layer near the symmetry plane slows the accumulation of low inertia fluid on that plane. These two factors may be summarised as: the large azimuthal pressure gradient in the relatively thin boundary layer on the flank reduces the convergence of fluid on the suction side of the symmetry plane, as predicted by potential theory; and the small pressure gradient in a thick boundary layer delays the accumulation of low inertia fluid, thus allowing an extended length of attached flow despite a considerable length of adverse streamwise pressure gradient.

High precision in the surface pressure measurements combined with measurements at a series of Reynolds numbers allowed the identification of changes in the surface pressure distribution due to thickening boundary layers, laminar-turbulent boundary layer transition, laminar sep-

aration bubbles and turbulent flow separation. Also identified in certain regions was a very small spread in the surface pressure distribution with Reynolds number. This spread occurred in regions of laminar flow and high azimuthal pressure gradient. This spread was very small and probably has negligible influence on the overall flow around the spheroid or ellipsoid.

The explanation for this spread was based on the azimuthal pressure gradient having a greater influence on the direction of flow in the thicker boundary layer that exists at smaller Reynolds numbers. This change in flow direction in turn has a very small influence, that varies according to boundary layer thickness, on the static pressure variation across the boundary layer and thus the surface pressure. It will be interesting if future experimental or computational studies confirm the existence of this spread and the explanation provided.

The wake survey for the 4.2–2–1 ellipsoid at an incidence of -10.2° showed one major flow structure. This vortical structure was generated due to the pressure difference between the pressure and suction side. The CFD was used to examine the possible interaction of this structure and the flow from the flank separation.

The experimental work completed in this research was obtained for a range of Reynolds numbers encompassing transcritical flow conditions. Measurements in these conditions are very sensitive to minor influences. For this reason care has been taken to examine the measurements for consistency across the range of measurement types. Measurements were taken over a large number of closely spaced Reynolds numbers to identify trends.

Since the commencement of this research the consideration of transition in commercial finite volume codes has been facilitated by the introduction of the correlation based technique of Menter et al. [92]. The present study could not compare the measured results with predictions of this transition model, as parts of the correlation model are not available in the open literature.

The trends and salient flow features identified and quantitative measurements in this research are intended to provide a means to assess the suitability of CFD codes applied to UUVs. This application is difficult as the flow around the hull exhibits boundary layer transition and boundary layer separation from curved surfaces. Particular attention has been directed to the boundary layer separation and pressure recovery at the rear of the models. Accurate calculation of boundary layer separation and surface pressure distribution in this region is critical to determine drag. This parameter is important to calculate precisely in order to obtain reasonable estimates of the range, power requirements and speed of UUVs.

On the pressure side using a fully turbulent boundary layer resulted in boundary layer separation upstream of the location measured. Implementing a laminar region extended the length of attached boundary layer on the pressure side at the higher Re , examined, but not to the extent observed in the measurements.

At the lower Reynolds numbers the implementation of the laminar regions tended to result in either a laminar separation upstream of the transition region, or a short separation bubble in the transition region. Implementation of the laminar region at the lower Reynolds numbers examined required minor modifications to the location of the transition region and provided limited improvement of the results. The primary impediment to the implementation of laminar regions was the separation of the laminar boundary layer upstream of the transition region. Although the implementation of the measured laminar regions in the CFD had limited success it is necessary to allow for the laminar regions if important features of the transcritical flow are to be calculated. These studies demonstrated the importance of correctly modelling the position and length of the transition region. Although the two-equation turbulence models used without laminar regions are obviously unable to calculate any of the features associated with transcritical flow, they provide good agreement with the measured surface pressure distributions, surface streamlines and wake examined at the larger Reynolds numbers studied. It is inevitable that these models will miss important features associated with the separation of the laminar boundary layer at the smaller Reynolds numbers.

The implementation of laminar regions provided occasional improvement, demonstrating the value of allowing for transitional flow in CFD calculations. Measurements such as those presented in the present research are necessary to assess the performance of computational techniques able to incorporate such capability into the turbulence modelling.

In the course of this research several experimental techniques were refined that other workers may find useful. These include:

- A method for creating discrete element trip strips for promoting turbulent boundary layers. A standard method of creating these elements using epoxy [59] was found to be problematic and slow; particularly on doubly curved surfaces. A substitute technique using self-adhesive PVC sheet was developed. Once the small circular elements were cut into the centre of a long thin vinyl strip the strip could be applied to the model. The excess material was then peeled off carefully to ensure the circular elements were left on the surface. Using this technique a trip strip could be applied to a model in situ in around half an hour. The major difficulty with this technique was finding a sign writer willing and able to cut such small elements. A range of material thickness is available, up to a maximum of about 0.15 mm . This technique allows for very uniform distribution and height of the elements. The elements were found to have excellent adhesion to stainless steel, aluminium and PVC.
- A technique using silicone oil over a very broad range of viscosity, mixed with titanium white for on-body visualisation. This mixture had the advantage that its viscosity can be

adjusted for a range of conditions. It has close to neutral buoyancy in water, so gravity has negligible impact on the visualisation. Another requirement for this mixture was that it should not damage the expensive acrylic windows used in the test section, as a hydrocarbon based substance might.

- Modifications were made to a fast response total pressure probe. These modifications reduced the effective mass experienced by the transducer diaphragm, thus improving the frequency response. This modification also improved the repeatability of manufacture of these probes.

Future research in this field could include surface shear stress measurements and a greater range of off-body measurements including: velocity profiles through the boundary layer; a series of wake surveys at different streamwise locations; and PIV in the wake. An examination of the static and dynamic roll characteristics of flatfish type bodies and the resulting flow structures, as originally intended for this study, would also be a valuable addition to the literature.